J. Fluid Mech. (2019), *vol.* 876, *pp.* 288–325.
doi:10.1017/jfm.2019.546

Effects of nozzle-exit boundary-layer profile on the initial shear-layer instability, flow field and noise of subsonic jets

Christophe Bogey[1,†] **and Roberto Sabatini**[2]

[1]Univ Lyon, Ecole Centrale de Lyon, INSA Lyon, Université Claude Bernard Lyon I, CNRS, Laboratoire de Mécanique des Fluides et d'Acoustique, UMR 5509, F-69134, Ecully, France

[2]Departement of Physical Sciences, Embry-Riddle Aeronautical University, Daytona Beach, 32114 Florida, USA

(Received 1 March 2019; revised 24 June 2019; accepted 1 July 2019)

The influence of the nozzle-exit boundary-layer profile on high-subsonic jets is investigated by performing compressible large-eddy simulations (LES) for three isothermal jets at a Mach number of 0.9 and a diameter-based Reynolds number of 5×10^4, and by conducting linear stability analyses from the mean-flow fields. At the exit section of a pipe nozzle, the jets exhibit boundary layers of momentum thickness of approximately 2.8 % of the nozzle radius and a peak value of turbulence intensity of 6 %. The boundary-layer shape factors, however, vary and are equal to 2.29, 1.96 and 1.71. The LES flow and sound fields differ significantly between the first jet with a laminar mean exit velocity profile and the two others with transitional profiles. They are close to each other in these two cases, suggesting that similar results would also be obtained for a jet with a turbulent profile. For the two jets with non-laminar profiles, the instability waves in the near-nozzle region emerge at higher frequencies, the mixing layers spread more slowly and contain weaker low-frequency velocity fluctuations and the noise levels in the acoustic field are lower by 2–3 dB compared to the laminar case. These trends can be explained by the linear stability analyses. For the laminar boundary-layer profile, the initial shear-layer instability waves are most strongly amplified at a momentum-thickness-based Strouhal number $St_\theta = 0.018$, which is very similar to the value obtained downstream in the mixing-layer velocity profiles. For the transitional profiles, on the contrary, they predominantly grow at higher Strouhal numbers, around $St_\theta = 0.026$ and 0.032, respectively. As a consequence, the instability waves rapidly vanish during the boundary-layer/shear-layer transition in the latter cases, but continue to grow over a large distance from the nozzle in the former case, leading to persistent large-scale coherent structures in the mixing layers for the jet with a laminar exit velocity profile.

Key words: jet noise, boundary layer separation, free shear layers

† Email address for correspondence: christophe.bogey@ec-lyon.fr

1. Introduction

There has been a considerable number of studies on the effects of the initial conditions on free shear layers and jets for more than five decades. In particular, great attention has been paid to the state of the nozzle-exit boundary layer, which may vary from one experiment to another depending on the facility characteristics and on the nozzle diameter and geometry. For instance, the jets are often initially laminar in small-scale experiments, whereas they are initially turbulent in full-scale experiments. In order to make meaningful comparisons, it can therefore be necessary to trip the boundary layer in the nozzle in order to generate turbulent exit conditions, as was the case in the pioneering work of Bradshaw (1966) and Crow & Champagne (1971).

The differences obtained between initially laminar and initially turbulent shear layers and jets have been described in a long list of papers. In the laminar case, instability waves are amplified just downstream of the nozzle at a preferred momentum-thickness-based Strouhal number equal to $St_\theta = 0.017$ according to the linear stability analyses conducted from hyperbolic–tangent velocity profiles (Michalke 1984), and varying within the range $0.009 \leqslant St_\theta \leqslant 0.018$ in experiments (Sato 1971; Zaman & Hussain 1981; Gutmark & Ho 1983). The shear layers subsequently roll up to form essentially two-dimensional vortical structures, whose interactions result in three-dimensional turbulence. The levels of velocity fluctuations rapidly increase and reach a sharp peak during that laminar–turbulent transition. In the initially turbulent case, on the contrary, they grow monotonically and very slowly from the nozzle exit (Bradshaw 1966; Hill, Jenkins & Gilbert 1976; Hussain & Zedan 1978*b*; Browand & Latigo 1979; Husain & Hussain 1979). Moreover, the jet flow development is faster in the laminar case than in the turbulent case, leading to a shorter potential core and a higher rate of centreline velocity decay (Hill *et al.* 1976; Raman, Zaman & Rice 1989; Russ & Strykowski 1993; Raman, Rice & Reshotko 1994; Xu & Antonia 2002). The impact of the nozzle-exit boundary-layer state is also significant on jet noise sources, as reported in the review papers by Crighton (1981) and Lilley (1994). It has notably been established in Maestrello & McDaid (1971), Zaman (1985*a*,*b*) and Bridges & Hussain (1987) that initially laminar jets emit more noise than initially turbulent jets, and that the additional acoustic components can be attributed to the pairings of the two-dimensional vortices induced by the laminar–turbulent transition in the shear layers. After the transition, coherent, well-organized turbulent structures appear to persist, as revealed by the experiments of Brown & Roshko (1974) and Wygnanski *et al.* (1979). The presence of coherent structures in initially turbulent mixing layers is less obvious according to Chandrsuda *et al.* (1978), but is supported by the measurements in such flows of a peak Strouhal number of $St_\theta = 0.022$–0.028 by Drubka & Nagib (1981), Hussain & Zaman (1985) and Morris & Foss (2003). The reasons for these values of Strouhal number well above those obtained for initially laminar flow conditions remain however unexplained, as was noted by Ho & Huerre (1984).

The issue of jet initial conditions has recently received renewed attention in the aeroacoustics community since Viswanathan (2004) stated that the jet far-field measurements of Tanna (1977) might be contaminated by spurious facility noise. In reply to this, Harper-Bourne (2010) suggested that the extra components emerging at high frequencies in Tanna's (1977) sound spectra are due to laminar flow conditions at the nozzle exit. This seems to be confirmed by the experimental results obtained by Viswanathan & Clark (2004), Zaman (2012) and Karon & Ahuja (2013) for high-subsonic jets exhausting from two nozzles of different internal profiles, namely

Reference	Case	Re_D	H	δ_θ/r_0	Re_θ	u'_e/u_j (%)
Zaman (2012)	ASME, $M = 0.37$	2.2×10^5	(Laminar)	0.0050	556	11.5
	Conical, $M = 0.37$	2.2×10^5	(Turbulent)	0.0106	1179	7
Karon & Ahuja (2013)	ASME, $M = 0.40$	3.5×10^5	2.34	0.0049	870	—
	Conical, $M = 0.40$	3.5×10^5	1.71	0.0065	1135	—
Fontaine *et al.* (2015)	Short nozzle	6.6×10^5	2.18	0.0109	3620	14
	Medium nozzle	6.6×10^5	1.53	0.0307	10 180	13
	Long nozzle	6.6×10^5	1.47	0.0426	14 030	12
Brès *et al.* (2018)	Baseline_LES_10M	10^6	2.54	0.0102	5100	6
	BL16M_WM_Turb	10^6	1.55	0.0142	7100	13
Morris & Foss (2003)	Turb. boundary layer	—	1.31	—	4650	—

TABLE 1. Flow conditions at the nozzle exit for round jets (Zaman 2012; Karon & Ahuja 2013; Fontaine *et al.* 2015; Brès *et al.* 2018) and at the separation point created using a sharp edge for a turbulent boundary layer (Morris & Foss 2003).

the ASME and the conical nozzles. Indeed, more noise is measured with the ASME nozzle than with the conical nozzle, that is, for highly disturbed, nominally laminar boundary layers than for turbulent boundary layers; refer to the nozzle-exit conditions of table 1. For instance, for the jet at a Mach number of 0.896 considered by Zaman (2012), the sound levels with the ASME nozzle are stronger by 2–3 dB for diameter-based Strouhal numbers $St_D \geqslant 0.3$ at all radiation angles, and approximately by 1 dB for lower frequencies at angles between 60° and 90° with respect to the flow direction. On the basis of flow visualizations, Zaman (2017) related this to the perseverance of organized coherent structures in the shear layers of the jets issuing from the ASME nozzle. Similarly, in the experiment of Fontaine *et al.* (2015) who explored the shear-layer flow properties and the noise of three initially highly disturbed jets with different nozzle-exit conditions, given in table 1, the jet from the small nozzle with a partially developed boundary layer generates 3 dB more intense sound than the two jets from the medium and large nozzles with fully turbulent boundary layers. In addition, the peak turbulence intensities a few diameters downstream of the nozzle exit are stronger for the first jet.

The relative importance of each of the nozzle-exit parameters in the above results is difficult to distinguish, because these parameters usually vary simultaneously, as illustrated in table 1. When the nozzle-exit flow conditions become turbulent, with or without boundary-layer tripping, the shape factor of the boundary-layer profile decreases. This factor, defined as $H = \delta^*/\delta_\theta$ where δ^* and δ_θ are the boundary-layer displacement and momentum thickness, takes values of around 2.5 for laminar profiles and 1.4 for turbulent profiles. At the same time, the boundary-layer thickness increases, and the nozzle-exit peak turbulence intensities u'_e/u_j, where u'_e and u_j are the maximum root mean square (r.m.s.) value of the velocity fluctuations and the jet velocity, most often grow. In some experiments, similar turbulence levels are obtained, as, for instance, in the work of Morris & Zaman (2009) where values of u'_e/u_j equal to 6.7 % and 7.5 % are reported for untripped and tripped jets at a diameter-based Reynolds number $Re_D = 3 \times 10^5$. It even happens that the velocity fluctuations are larger in laminar than in turbulent nozzle-exit boundary layers. Examples of this counter-intuitive tendency have been given by Raman *et al.* (1989, 1994) for

tripped/untripped jets and by Zaman (2012) who measured values of u'_e/u_j around 11 % using the ASME nozzle but around 7 % using the conical nozzle for jets at $2 \times 10^5 \leqslant Re_D \leqslant 6 \times 10^5$, see the values for $Re_D = 2.2 \times 10^5$ in table 1. In that case, the effects of the velocity profile and those of the turbulence levels are likely to counteract each other, which may result in some confusion.

Therefore, there is clearly a need to study the influence of the nozzle-exit boundary-layer profile with all other exit parameters held constant. For this, it seems worthwhile to use unsteady compressible simulations, which have made spectacular progress over the last three decades, and now allow us to conduct investigations under controlled conditions. Large-eddy simulations (LES) have for instance been run by the first author over the last decade (Bogey & Bailly 2010; Bogey, Marsden & Bailly 2011*b*,*c*, 2012*a*,*b*; Bogey & Marsden 2013; Bogey 2018) to investigate the impact of nozzle-exit conditions on initially laminar and highly disturbed subsonic round jets. Due to limitations in computing resources, the jets had moderate Reynolds numbers Re_D of between 2.5×10^4 and 2×10^5, and all exhibited laminar mean velocity profiles at the nozzle exit, in order to ensure numerical accuracy. Subsonic jets with tripped boundary layers have also been recently calculated by an increasing number of other researchers, including Lorteau, Cléro & Vuillot (2015) and Zhu *et al.* (2018), among others. Specifically concerning initially turbulent jets, the first attempts of computation have been made by Bogey, Barré & Bailly (2008) and Uzun & Hussaini (2007). However, the grid was too coarse in the former case, while its spatial extent was limited to 4.5 diameters downstream of the nozzle in the latter. Later, Sandberg, Sandham & Suponitsky (2012) carried out a simulation of a fully turbulent pipe flow at $Re_D = 7500$ exiting into a coflow, and Bühler, Kleiser & Bogey (2014) successfully computed a jet at $Re_D = 18\,100$ with turbulent conditions at the exit of a pipe nozzle. None of these studies however addresses the question of the mean velocity profile. More recently, two jets at $Re_D = 2 \times 10^5$ with nozzle-exit conditions roughly matching those found in experiments using the ASME and the conical nozzles have been performed by Bogey & Marsden (2016). Unfortunately, the results for the two jets are very similar, suggesting that the jet initial conditions in the simulations do not adequately reflect those in the experiments. Finally, Brès *et al.* (2018) calculated two isothermal subsonic jets at $Re_D = 10^6$ with initially laminar and turbulent nozzle-exit boundary layers, as indicated in table 1. The initially laminar jet radiates greater high-frequency noise than the initially turbulent jet, which was attributed to the fact that the instability waves in the near-nozzle region grow at different rates in the two jets.

In the present work, the influence of the nozzle-exit boundary-layer profile on high-subsonic jets is investigated by combining well-resolved large-eddy simulations and linear stability analyses for three isothermal round jets at a Mach number $M = u_j/c_a = 0.9$ and a Reynolds number $Re_D = u_j D/\nu = 5 \times 10^4$, where c_a, D and ν are the speed of sound in the ambient medium, the jet diameter and the kinematic molecular viscosity. In order to consider the effects of the mean velocity profile alone, momentum boundary-layer thicknesses of $\delta_\theta \simeq 0.028 r_0$ and peak turbulence intensities of $u'_e/u_j \simeq 6\,\%$ are prescribed at the exit of a pipe nozzle for all jets. The boundary-layer profiles however vary, and are laminar in the first jet and transitional (partially developed) in the two others, with shape factors H ranging between 1.71 and 2.29. The first objective will be to determine whether the flow and sound fields of the jets show significant differences, and whether these differences correspond to those usually encountered between initially laminar and initially turbulent jets, namely a faster flow development, stronger velocity fluctuations in the mixing layers

	H	δ_θ/r_0	δ_{99}/r_0	α_{trip}
jetBL	2.55	0.0288	0.202	0.0460
jetT1	1.88	0.0288	0.215	0.0675
jetT2	1.52	0.0288	0.254	0.0830

TABLE 2. Shape factor H, momentum thickness δ_θ and 99 % velocity thickness δ_{99} of the boundary-layer profile at the pipe-nozzle inlet and strength of the trip-like excitation α_{trip}.

and more noise in the acoustic field in the laminar case. In particular, comparisons will be made with the trends observed in the experiments of Zaman (2012, 2017) using the ASME and the conical nozzles and of Fontaine *et al.* (2015), and in the simulations of Brès *et al.* (2018). They will be mostly qualitative due to the disparities in upstream flow conditions. The second objective will be to propose an explanation for the higher noise levels expected for a laminar boundary-layer profile. For that purpose, the development of the instability waves very near the nozzle exit and during the transition from a boundary layer to a shear layer will be detailed. It will also be discussed based on the linear stability analyses conducted from the mean-flow fields, as in Fontaine *et al.* (2015) and Brès *et al.* (2018). However, while the latter authors mainly focused on the amplification rates of the instability waves, the present study will specially examine the sensitivity of the unstable frequencies to the nozzle-exit velocity profile, previously noted by Drubka & Nagib (1981), Hussain & Zaman (1985) and Morris & Foss (2003) for shear layers, and its possible role in the discrepancies observed in the flow and sound fields of the jets.

The paper is organized as follows. The parameters of the three jets, of the large-eddy simulations, of the extrapolations of the LES acoustic near fields to the far field and of the linear stability analyses are documented in § 2. The nozzle-exit flow properties, the mixing-layer and jet flow fields and the jet acoustic fields are described in § 3. Concluding remarks are given in § 4. Finally, comparisons of the non-laminar nozzle-inlet velocity profiles imposed for two of the three jets with boundary-layer measurements are shown in appendix A, and results from a grid-refinement study are provided in appendix B.

2. Parameters

2.1. *Jet definition*

Three isothermal round jets at a Mach number $M = 0.9$ and a Reynolds number $Re_D = 5 \times 10^4$, referred to as jetBL, jetT1 and jetT2 in what follows, have been simulated. They originate at $z = 0$ from a pipe nozzle of radius r_0 and length $2r_0$, whose lip is $0.053r_0$ thick, into a medium at rest of temperature $T_a = 293$ K and pressure $p_a = 10^5$ Pa. At the pipe inlet, at $z = -2r_0$, different boundary-layer profiles, whose main characteristics are collected in table 2, are imposed for the axial velocity. Radial and azimuthal velocities are set to zero, pressure is equal to p_a and temperature is determined by a Crocco–Busemann relation.

The inlet axial velocity profiles are represented in figure 1(*a*). In jetBL, the profile is a Blasius laminar boundary-layer profile with a shape factor $H = \delta^*/\delta_\theta = 2.55$, where the boundary-layer displacement and momentum thickness are respectively defined as

$$\delta^* = \int_0^\infty \left(1 - \frac{\langle u_z \rangle}{\langle u_z \rangle (r = 0)}\right) \mathrm{d}r, \tag{2.1}$$

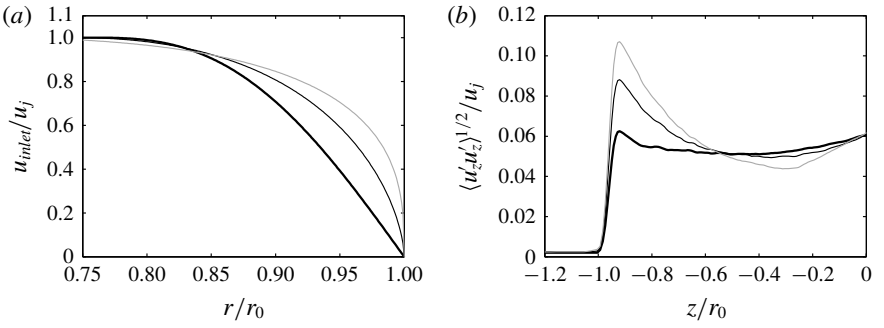

FIGURE 1. Representation (*a*) of the axial velocity profile u_{inlet} imposed at the pipe-nozzle inlet and (*b*) of the peak r.m.s. values of axial velocity fluctuations u_z' in the nozzle: ——— jetBL, —— jetT1, ——— jetT2.

and

$$\delta_\theta = \int_0^\infty \frac{\langle u_z \rangle}{\langle u_z \rangle (r=0)} \left(1 - \frac{\langle u_z \rangle}{\langle u_z \rangle (r=0)}\right) \mathrm{d}r. \tag{2.2}$$

The Blasius profile is given by the Pohlhausen's fourth-order polynomial approximation

$$\frac{u_{inlet}(r)}{u_j} = \begin{cases} \dfrac{(r_0 - r)}{\delta_{BL}} \left[2 - 2\left(\dfrac{(r_0 - r)}{\delta_{BL}}\right)^2 + \left(\dfrac{r_0 - r}{\delta_{BL}}\right)^3\right] & \text{if } r \geqslant r_0 - \delta_{BL} \\ 1 \quad \text{otherwise,} \end{cases} \tag{2.3}$$

where δ_{BL} is the boundary-layer thickness.

In jetT1 and jetT2, the inlet profiles are transitional boundary-layer profiles with $H = 1.88$ and 1.52, respectively. They are derived from the turbulent profile proposed by De Chant (2005), and defined as

$$\frac{u_{inlet}(r)}{u_j} = \begin{cases} \left(\sin\left[\dfrac{\pi}{2}\left(\dfrac{r_0 - r}{\delta_{T_i}}\right)^{\beta_i}\right]\right)^{\gamma_i} & \text{if } r \geqslant r_0 - \delta_{T_i} \\ 1 \quad \text{otherwise,} \end{cases} \tag{2.4}$$

where δ_{T_i} is the boundary-layer thickness, and the values of the exponents β_i and γ_i are equal to $\beta_1 = 0.464$ and $\gamma_1 = 1.32$, and to $\beta_2 = 0.423$ and $\gamma_2 = 0.82$. Considering the strong similarities between the near-wall mean-flow statistics obtained for turbulent pipe and boundary-layer flows (Monty *et al.* 2009), they have been designed to fit the experimental data provided by Schubauer & Klebanoff (1955) for a flat-plate boundary layer in the region of changeover from laminar to fully turbulent conditions, as shown in appendix A.

In the three jets, the inlet boundary-layer thicknesses are arbitrarily set to $\delta_{BL} = 0.25 r_0$ in jetBL, $\delta_{T_1} = 1.043\delta_{BL} = 0.26 r_0$ in JetT1 and $\delta_{T_2} = 1.328\delta_{BL} = 0.33 r_0$ in JetT2, in order to obtain a momentum thickness of $\delta_\theta = 0.0288 r_0$ in all cases. The associated 99 % velocity thicknesses δ_{99} thus vary from $0.202 r_0$ in jetBL up to $0.254 r_0$ in jetT2. With respect to the experiments of Zaman (2012) and Karon & Ahuja (2013), see in table 1, the boundary layers in the present jets are thicker to guarantee a high

numerical accuracy, as will be discussed in § 2.3 and in appendix B. Given the jet Reynolds number of $Re_D = 5 \times 10^4$, chosen to perform very well resolved LES, this also leads to a momentum-thickness-based Reynolds number of $Re_\theta = u_j \delta_\theta / \nu = 720$, which is comparable to the values measured in the experiments. This is of importance because Re_θ is a key parameter in developing shear layers (Hussain & Zedan 1978*b*; Bogey & Marsden 2013).

In order to generate disturbed upstream conditions for the jets, which otherwise would initially contain negligible velocity fluctuations, the boundary layers are 'tripped' in the pipe using an arbitrary forcing whose parameters are determined by trial and error (Klebanoff & Diehl 1952; Coles 1962; Erm & Joubert 1991; Castillo & Johansson 2012; Hutchings 2012; Schlatter & Örlü 2012). In simulations, forcing devices of different kinds have been proposed. A small step can for instance be mounted on the wall inside the nozzle. Random fluctuations, synthetic turbulence or instability modes can alternatively be imposed on the flow profiles. In the present jets, the forcing procedure detailed in appendix A of Bogey *et al.* (2011*b*) is implemented. It consists in adding random low-level vortical disturbances uncorrelated in the azimuthal direction in the boundary layers. It has been previously used for both laminar (Bogey *et al.* 2011*b*, 2012*a*,*b*; Bogey & Marsden 2013) and non-laminar (Bogey & Marsden 2016) boundary-layer profiles. The forcing is applied at the axial position $z = -0.95 r_0$ and at the radial position of $r = r_0 - \delta_{BL}/2 = 0.875 r_0$ in all cases. However, the forcing magnitudes are not the same, and have been adjusted after preliminary tests to obtain peak nozzle-exit turbulence intensities u'_e/u_j of 6 % for all jets. This level is close to those measured by Zaman (2012) just downstream of the conical nozzle for initially turbulent jets, refer to table 1 for instance. The values of the coefficient α_{trip} setting the maximum value of the added velocity fluctuations to $\alpha_{trip} u_j$, hence specifying the forcing strength, are given in table 2. They are equal to 0.046, 0.0675 and 0.083 in jetBL, jetT1 and jetT2, respectively. Consequently, the lower the inlet boundary-layer shape factor, the higher the amplitude of the excitation necessary to reach $u'_e/u_j = 6\,\%$, This is illustrated in figure 1(*b*) showing the variations of the maximum r.m.s. value of axial velocity fluctuations in the pipe.

As pointed out above, there exit some discrepancies between the nozzle-exit conditions of the present jets and of the experiments of table 1 in terms of Re_D and ratio δ_θ / r_0. The higher value of δ_θ / r_0 in the simulations, in particular, will result in lower frequencies in the shear layers just downstream of the nozzle. Thanks to the similarities in Re_θ and u'_e/u_j, the physical mechanisms at play in this zone can yet be expected to be of the same nature as those in the experiments using the ASME and conical nozzles. Performing qualitative comparisons with the trends revealed in these experiments therefore appears relevant. Quantitative comparisons with measurements for reference jets of the literature will also be made throughout the paper. They are given mainly for illustration purposes, because these jets have Reynolds numbers $Re_D \simeq 10^6$ and certainly very thin nozzle-exit boundary layers. In addition, they are most likely initially fully turbulent, and such a case is not considered in this study. It is however hoped that on the basis of the differences obtained between jetT1 and jetT2, results for a more turbulent boundary-layer profile could be extrapolated. Finally, the experimental jets all exhaust for a convergent nozzle, leading to a pressure gradient at the nozzle exit whose effects are unclear (Zaman 2012), which is not taken into account in the simulations.

$N_r \times N_\theta \times N_z$	$\Delta r/r_0$	$(r_0\Delta\theta)/r_0$	$\Delta z/r_0$	L_r/r_0	L_z/r_0	Tu_j/r_0
$504 \times 1024 \times 2085$	0.36 %	0.61 %	0.72 %	15	40	500

TABLE 3. Numbers of grid points N_r, N_θ and N_z, mesh spacings Δr at $r = r_0$, $r_0\Delta\theta$ and Δz at $z = 0$, extents of the physical domain L_r and L_z and simulation time T after the transient period.

2.2. *LES numerical methods*

For the LES, the numerical framework is identical to that used in previous jet simulations (Bogey & Bailly 2010; Bogey *et al.* 2011*b*, 2012*a*,*b*; Bogey & Marsden 2013; Bogey 2018). They are carried out using an in-house solver of the three-dimensional filtered compressible Navier–Stokes equations in cylindrical coordinates (r, θ, z) based on low-dissipation and low-dispersion explicit schemes. The axis singularity is taken into account by the method of Mohseni & Colonius (2000). In order to alleviate the time-step restriction near the cylindrical origin, the derivatives in the azimuthal direction around the axis are calculated at coarser resolutions than permitted by the grid (Bogey, de Cacqueray & Bailly 2011*a*). For the points closest to the jet axis, they are evaluated using 16 points, yielding an effective resolution of $2\pi/16$. Fourth-order eleven-point centred finite differences are used for spatial discretization, and a second-order six-stage Runge–Kutta algorithm is implemented for time integration (Bogey & Bailly 2004). A sixth-order eleven-point centred filter (Bogey, de Cacqueray & Bailly 2009*b*) is applied explicitly to the flow variables every time step. Non-centred finite differences and filters are also used near the pipe walls and the grid boundaries (Berland *et al.* 2007; Bogey & Bailly 2010). At the boundaries, the radiation conditions of Tam & Dong (1996) are applied, with the addition at the outflow of a sponge zone combining grid stretching and Laplacian filtering (Bogey & Bailly 2002). At the inflow and radial boundaries, density and pressure are also brought back close to p_a and ρ_a every $0.055r_0/c_a$ at rate of 0.5 %, in order to keep the mean values of density and pressure around their ambient values without generating significant acoustic reflections. No co-flow is imposed.

In the present large-eddy simulations, the explicit filtering is employed to remove grid-to-grid oscillations, but also as a subgrid-scale high-order dissipation model in order to relax turbulent energy from scales at wavenumbers close to the grid cutoff wavenumber while leaving larger scales mostly unaffected. The performance of this LES approach has been assessed in past studies for subsonic jets, Taylor–Green vortices and turbulent channel flows (Bogey & Bailly 2006, 2009; Bogey *et al.* 2011*b*; Fauconnier, Bogey & Dick 2013; Kremer & Bogey 2015), from comparisons with the solutions of direct numerical simulations and from the examination of the magnitude and the properties of the filtering dissipation in the wavenumber space.

2.3. *Simulation parameters*

The grid used in the present jet simulations is detailed and referred to as gridz40B in a recent grid-sensitivity study of the flow and acoustic fields of an initially highly disturbed isothermal round jet at $M = 0.9$ and $Re_D = 10^5$ (Bogey 2018). As indicated in table 3, it contains $N_r \times N_\theta \times N_z = 504 \times 1024 \times 2048 = 10^9$ points. It extends radially out to $L_r = 15r_0$ and axially, excluding the 100-point outflow sponge zone, down to $L_z = 40r_0$. There are 169 points along the pipe nozzle between $z = -2r_0$ and

	Δr^+	$(r_0\Delta\theta)^+$	Δz^+
JetBL	1.4	2.4	2.8
JetT1	2.1	3.6	4.3
JetT2	2.7	4.6	5.4

TABLE 4. Near-wall mesh spacings Δr, $r_0\Delta\theta$ and Δz given in wall units based on the wall friction velocity u_τ at the nozzle exit.

0, 96 points between $r=0$ and r_0 and 41 points between $r=r_0-\delta_{BL}=0.75r_0$ and r_0. In the radial direction, the mesh spacing Δr is minimum and equal to $0.0036r_0$ at $r=r_0$, and is equal to $0.0141r_0$ at $r=0$, $0.0148r_0$ at $r=2r_0$, $0.0335r_0$ at $r=4r_0$ and $0.075r_0$ between $r=6.25r_0$ and L_r. The latter mesh spacing leads to a diameter-based Strouhal number of $St_D=f\,D/u_j=5.9$ for an acoustic wave discretized by five points per wavelength, where f is the frequency. In the axial direction, the mesh spacing Δz is minimum and equal to $0.0072r_0$ between $z=-r_0$ and 0, and increases at a stretching rate of 0.103 % farther downstream to reach $0.0127r_0$ at $z=5r_0$, $0.0178r_0$ at $z=10r_0$, $0.0230r_0$ at $z=15r_0$ and $0.0488r_0$ at $z=L_z$.

The quality of gridz40B has been shown in Bogey (2018) for a jet at $Re_D=10^5$ characterized, at the nozzle exit, by a laminar Blasius boundary layer of thickness $\delta_{BL}=0.15r_0$ and a peak turbulence intensity of $u'_e/u_j=9\,\%$. Therefore, it is highly likely that in the present work, the grid resolution is appropriate for jetBL at $Re_D=5\times10^4$ with $\delta_{BL}=0.25r_0$ and $u'_e/u_j=6\,\%$. For jetT1 and jetT2 with non-laminar boundary-layer profiles, the suitability of the grid is less obvious. In order to address this issue, the near-wall mesh spacings in the pipe expressed in wall units based on the wall friction velocity at the nozzle exit are provided in table 4. They are such that $\Delta r^+\leqslant 2.7$, $(r_0\Delta\theta)^+\leqslant 4.6$ and $\Delta z^+\leqslant 5.4$. The azimuthal and axial mesh spacings meet the requirements needed to compute turbulent wall-bounded flows accurately using direct numerical simulation (Kim, Moin, & Moser 1987; Spalart 1988) or LES involving relaxation filtering (Gloerfelt & Berland 2012; Kremer & Bogey 2015). On the contrary, the wall-normal spacing is two or three times larger than the recommended value of $\Delta r^+=1$. For the simulation of an initially fully turbulent jet, refining the wall-normal region by a factor of at least three would therefore be necessary, which would increase by the same amount the computational cost due to the explicit time-integration scheme. For the initially transitional jets considered in this paper, the sensitivity to the wall-normal spacing has however been assessed in a preliminary study using two shorter grids extending axially, excluding the outflow sponge zones, only down to $z=4r_0$ in order to save computational time. The coarsest of the two grids coincides with gridz40B in the boundary-layer region. The finest one is also identical to the latter in that region in the directions θ and z, but differs in the radial direction with $\Delta r/r_0=0.18\,\%$, instead of $\Delta r/r_0=0.36\,\%$, at $r=r_0$. The tripping procedure is exactly the same in all cases, but the time step is twice as small in the LES using the finest grid because of the numerical stability condition, leading to an application of the relaxation filtering that is twice as frequent. The mean and fluctuating velocity profiles obtained at the nozzle exit using the two grids, represented in appendix B for jetT2, are superimposed. This demonstrates that the LES solutions in the pipe do not depend on the radial mesh spacing at $r=r_0$ or on the relaxation filtering.

In the three jet LES, the time step is defined by $\Delta t=0.7\times\Delta r(r=r_0)/c_a$, yielding $\Delta t=0.0023\times r_0/u_j$. After a transient period of $275r_0/u_j$, the simulation time T,

given in table 3, is equal to $500r_0/u_j$. During that time period, the signals of density, velocities and pressure obtained on the jet axis at $r = 0$, on the cylindrical surfaces located at $r = r_0$ and $r = L_r = 15r_0$ and in the cross-sections at $z = -1.5r_0$, $z = 0$ and $z = L_z = 40r_0$, are recorded at a sampling frequency allowing spectra to be computed up to $St_D = 12.8$. The signals obtained in the four azimuthal planes at $\theta = 0$, $\pi/4$, $\pi/2$ and $3\pi/4$ are also stored, but at a halved frequency in order to reduce storage requirements. Finally, the Fourier coefficients estimated over the full section (r, z) for the first nine azimuthal modes for density, velocities and pressure are similarly saved. The flow and acoustic near-field statistics presented in the next sections are calculated from these recordings. They are averaged in the azimuthal direction, when possible. Time spectra are evaluated from overlapping samples of duration $45r_0/u_j$ on the jet axis, and $90r_0/u_j$ otherwise. In the azimuthal direction, post-processing can be performed up to the mode $n_\theta = 128$, where n_θ is the dimensionless azimuthal wavenumber such that $n_\theta = k_\theta r$.

Finally, the simulations required 200 GB of memory and have run for 340 000 iterations each. They have been performed using an OpenMP-based in-house solver on single nodes with 256 GB of memory, consisting of four Intel Sandy Bridge E5-4650 8-core processors at a clock speed of 2.7 GHz or of two Intel Xeon CPU E5-2670v3 8-core processors at 2.6 GHz. The time per iteration is approximately equal to 120 s in the first case using 32 cores and to 140 s in the second case using 16 cores, leading to the consumption of 1070 and 620 CPU hours, respectively, for 1000 iterations. Therefore, a total number of the order of 1 billion computational hours has been necessary for the full study.

2.4. *Linear stability analysis*

Inviscid spatial stability analyses have been carried out from the mean flow fields of the jets, as was done in previous investigations (Fontaine *et al.* 2015; Brès *et al.* 2018). More precisely, the compressible Rayleigh equation (Michalke 1984; Sabatini & Bailly 2015) has been solved for the LES profiles of mean axial velocity and mean density, locally considered parallel, from $z = 0.02r_0$ down to $z = 5r_0$. Viscous effects are not taken into account because they are expected to be very weak at the Reynolds numbers $Re_\theta \gtrsim 700$ considered in this work (Morris 1976, 2010). For a given axial distance z and a given Strouhal number St_D, the compressible Rayleigh equation is solved through a shooting technique (Morris 2010), based on the Euler method for the integration step and on the secant method for the search of the complex wavenumber $k_z\delta_\theta$. The integration is performed on a grid with a spatial step of $0.0001r_0$, extending from the LES grid point closest to the jet axis at $r = 0.007r_0$ out to $r = 5r_0$. Since the present stability study is performed directly from the LES profiles, which may contain high-frequency noise in the near-nozzle region of high mean-flow gradients, the profiles and their radial derivatives are filtered using a sixth-order eleven-point centred filter (Bogey *et al.* 2009*b*). A cubic spline interpolation is then employed to calculate the mean-flow values on the aforesaid grid. It can be noted that, in order to check the sensitivity of the results to the filtering, a tenth-order eleven-point centred filter has also been used to smooth the LES profiles of jetT2, in the case which exhibits the strongest gradients. The eigenvalues $k_z\delta_\theta$ thus obtained are identical to those calculated using the sixth-order filter.

2.5. *Far-field extrapolation*

The LES near-field fluctuations have been propagated to the far field using an in-house OpenMP-based solver of the isentropic linearized Euler equations (ILEE) in

cylindrical coordinates, based on the same numerical methods as the LES (Bogey *et al.* 2009*a*; Bogey 2018). The extrapolations are carried out from the velocity and pressure fluctuations recorded on the cylindric surface at $r = L_r = 15r_0$ and on the axial sections at $z = -1.5r_0$ and $z = L_z = 40r_0$ over a time period of $500r_0/u_j$ during the jet simulations, at a sampling frequency corresponding to $St_D = 12.8$. They aim to provide the pressure waves radiated at a distance of $150r_0$ from the nozzle exit, where far-field acoustic conditions are expected to apply according to measurements (Ahuja, Tester & Tanna 1987; Viswanathan 2006), between the angles of $\phi = 15°$ and 165° relative to the jet direction.

In practice, in order to compute separately the downstream and the upstream acoustic fields, whose magnitudes strongly vary, two far-field extrapolations are performed on two different grids, yielding results for $15° \leqslant \phi \leqslant 90°$ and for $60° \leqslant \phi \leqslant 165°$, respectively. The two grids are identical in the radial and the azimuthal directions, with $N_r = 2058$ and $N_\theta = 256$. In the direction r, they extend from $r = 2.5r_0$ out to $r = 151r_0$ with a mesh spacing of $\Delta r = 0.075r_0$, and end with a 80-point sponge zone. In the axial direction, the two grids respectively contain $N_z = 2171$ and $N_z = 3111$ points, and extend, excluding the 80-point sponge zones implemented at the upstream and downstream boundaries, from $z = -6r_0$ up to $z = 146r_0$ and from $z = -146r_0$ up to $z = 76r_0$, with a mesh spacing of $\Delta z = 0.075r_0$. This mesh spacing, leading to a Strouhal number $St_D = 5.9$ for an acoustic wave discretized by five points per wavelength, is identical to that in the LES near field.

In the first computation, the LES fluctuations are imposed onto the extrapolation grid for $-1.5r_0 \leqslant z \leqslant L_z$ at $r = L_r = 15r_0$, for $2.5r_0 \leqslant r \leqslant L_r$ at $z = -1.5r_0$ and for $7.5r_0 \leqslant r \leqslant L_r$ at $z = L_z = 40r_0$. The opening angle relative to the flow direction, with the nozzle exit as origin, is $\phi = 10°$, which allows most of the downstream noise components to be taken into account. In the second computation, the LES data are imposed onto the extrapolation grid as in the first one at $z = -1.5r_0$ and at $r = L_r = 15r_0$, but only for $14r_0 \leqslant r \leqslant L_r$ at $z = L_z = 40r_0$. The opening angle is larger than in the first case in order to avoid the presence of aerodynamic disturbances (Arndt, Long & Glauser 1997) on the extrapolation surface, which might cause low-frequency spurious waves (Bogey & Bailly 2010) in the upstream direction where noise levels are much lower than in the downstream direction.

Each ILEE computation requires 105 or 150 GB of memory depending on the grid used, and lasts during 7700 iterations. This leads to a total number approximately of 25 000 CPU hours consumed using 16-core nodes based on Intel Xeon CPU E5-2670 processors at 2.6 GHz. Finally, the far-field spectra are evaluated from the pressure signals obtained at $150r_0$ from the nozzle exit during the final 6000 iterations of the computations, i.e. during nearly $470r_0/u_j$. Thus, for the peak Strouhal number of $St_D = 0.2$ emerging in the downstream direction, and for the lowest Strouhal number of $St_D = 0.075$ represented in § 3.4.2, the far-field signals contains 48 and 18 time periods, respectively. The statistical convergence of the results is furthermore increased by calculating the spectra using overlapping samples of duration $90r_0/u_j$, and by averaging in the azimuthal direction.

3. Results

3.1. *Jet flow initial conditions*

3.1.1. *Nozzle-exit boundary-layer properties*

The profiles of mean and r.m.s. axial velocities calculated at the nozzle exit are presented in figure 2. Their main properties are provided in table 5. In figure 2(*a*),

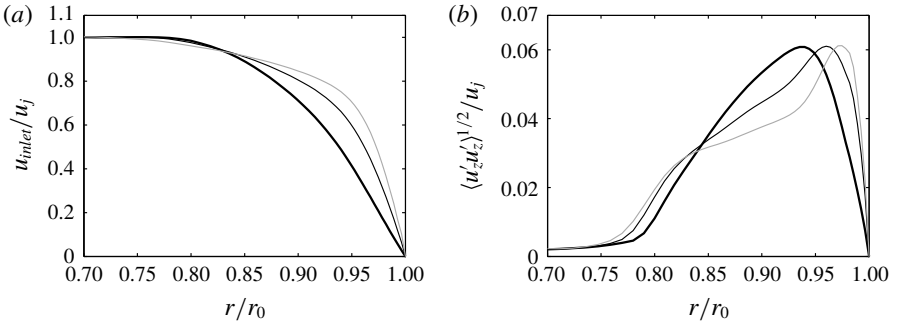

FIGURE 2. Radial profiles at the nozzle exit at $z = 0$ (*a*) of mean axial velocity $\langle u_z \rangle$ and (*b*) of the r.m.s. values of axial velocity fluctuations u_z': ——— jetBL, —— jetT1, ——— jetT2.

	H	δ_θ/r_0	δ_{99}/r_0	δ_ω/r_0	Re_θ	u_e'/u_j (%)	r_e/r_0	n_θ
JetBL	2.29	0.0299	0.210	0.118	747	6.08	0.935	50
JetT1	1.96	0.0280	0.220	0.062	700	6.10	0.960	51
JetT2	1.71	0.0274	0.241	0.043	685	6.12	0.975	64

TABLE 5. Nozzle-exit parameters: shape factor H, momentum thickness δ_θ, 99 % velocity thickness δ_{99} and vorticity thickness δ_ω of the boundary-layer profile, Reynolds number $Re_\theta = u_j\delta_\theta/\nu$, value u_e'/u_j and radial position r_e of peak axial turbulence intensity and peak azimuthal mode n_θ at $r = r_e$.

as intended, the mean velocity profiles differ significantly, and have shape factors H of 2.29 for jetBL, 1.96 for jetT1 and 1.71 for jetT2. The boundary-layer momentum thicknesses are similar, and range only from $\delta_\theta = 0.0299r_0$ for jetBL down to $\delta_\theta = 0.0274r_0$ for jetT2, leading to Reynolds numbers Re_θ between 685 and 747. From jetBL to jetT2, in addition, the 99 % velocity thickness δ_{99} increases slightly and the vorticity thickness $\delta_\omega = \langle u_z \rangle(r = 0)/\max(|\partial\langle u_z \rangle/\partial r|)$ evaluated from the maximum value of velocity gradient strongly decreases from $\delta_\omega = 0.118r_0$ down to $\delta_\omega = 0.043r_0$. The mean velocity profile for jetBL corresponds to a laminar boundary-layer profile, and, given that $H \simeq 1.45$ is obtained (Spalart 1988; Erm & Joubert 1991; Fernholz & Finley 1996; Schlatter & Örlü 2012) for fully developed boundary layers at $Re_\theta = 700$, the profiles for jetT1 and jetT2 are both transitional.

In figure 2(*b*), the peak turbulence intensities, imposed by the boundary-layer forcing, are all close to $u_e'/u_j = 6.1\,\%$. They are reached roughly at the positions of the maximum velocity gradients, hence move nearer to the wall from $r_e = 0.935r_0$ for jetBL up to $r_e = 0.975r_0$ for jetT2, as reported in table 5. The radial profile of r.m.s. velocity also changes with the boundary-layer shape. In the non-laminar cases, compared to the laminar case (Zaman 1985*a*,*b*), the peak is sharper and resembles that obtained in the inner region of turbulent boundary layers (Spalart 1988; Schlatter & Örlü 2012) as well as that measured just downstream of the nozzle lip for such flows (Morris & Foss 2003; Fontaine *et al.* 2015).

With respect to the parameters of the inlet boundary layers in table 2, the nozzle-exit parameters in table 5 are slightly different due to the flow development in the pipe between the forcing at $z = -0.95r_0$ and the exit at $z = 0$. The boundary layer has

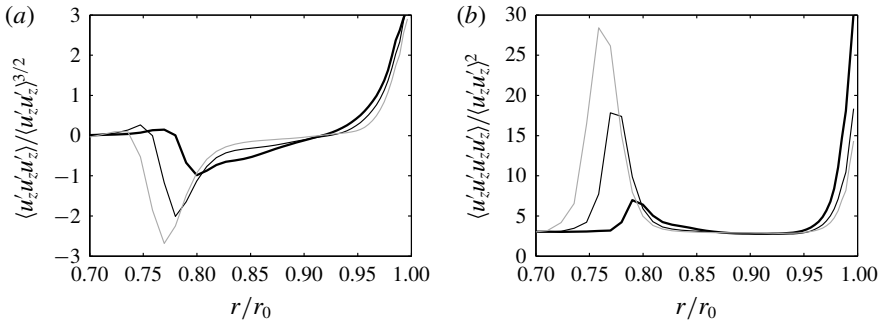

FIGURE 3. Radial profiles at the nozzle exit (a) of the skewness factor and (b) of the kurtosis factor of axial velocity fluctuations u'_z: ——— jetBL, —— jetT1, ——— jetT2.

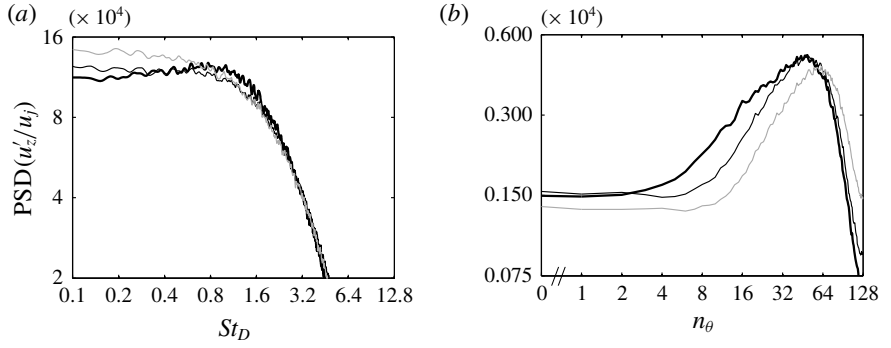

FIGURE 4. Power spectral densities (PSD) of axial velocity fluctuations u'_z obtained at the nozzle exit at the position $r = r_e$ of peak axial turbulence intensity, as a function (a) of Strouhal number St_D and (b) of azimuthal mode n_θ: ——— jetBL, —— jetT1, ——— jetT2.

a lower shape factor and a larger momentum thickness at the exit than at the pipe inlet for jetBL, whereas the opposite trends are observed for the two other jets.

The profiles of the skewness and kurtosis factors of the axial velocity fluctuations at $z = 0$ are depicted in figure 3. As expected, significant deviations from the values of 0 and 3 are found in the interfaces between the laminar inner-pipe region and the highly disturbed boundary layers, around $r = 0.75r_0$. They are stronger, in absolute value, as the mean velocity profile has a more turbulent shape, and indicate the occurrence of intermittent bursts of low-velocity fluid. In the boundary layers, the strongest deviations are obtained for the laminar case, close to the wall as well as on the high-speed side of the boundary layers. For instance, at $r = r_0 - \delta_{94} = 0.827r_0$ where δ_{94} is the 94 % velocity boundary-layer thickness, equal to $0.173r_0$ for all jets, the skewness values are of -0.65 for JetBL, -0.43 for JetT1 and -0.28 for JetT2. This tendency is in agreement with that obtained by Zaman (2017) who measured, also at $r = r_0 - \delta_{94}$, lower values of velocity skewness for nominally laminar nozzle-exit conditions than for turbulent ones.

The properties of the jet initial disturbances are examined by computing spectra of axial velocity fluctuations at the nozzle exit in both the inner and the outer boundary-layer regions. The spectra estimated in the inner region at the position $r = r_e$ of the turbulence intensity peak, i.e. between $r_e = 0.935r_0$ for jetBL and $r_e = 0.975r_0$ for jetT2, are represented as a function of the Strouhal number St_D in figure 4(a) and

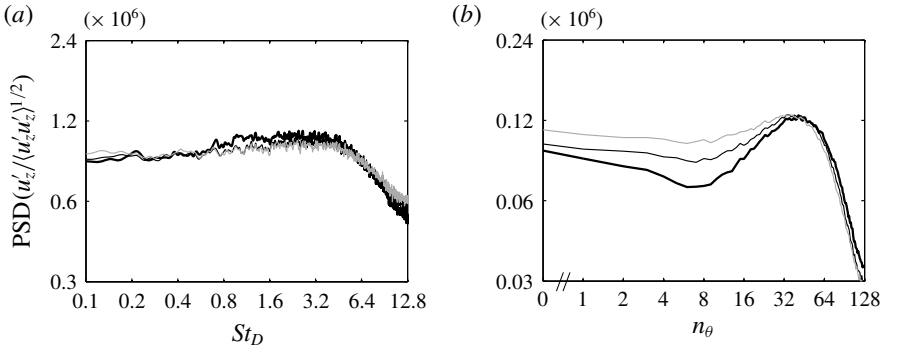

FIGURE 5. Power spectral densities of axial velocity fluctuations u_z' obtained at the nozzle exit at $r = r_0 - \delta_{94}$, as a function (*a*) of Strouhal number St_D and (*b*) of azimuthal mode n_θ: ——— jetBL, —— jetT1, ——— jetT2.

of the azimuthal mode n_θ in figure 4(*b*). Their shapes are roughly the same in the three cases, and correspond, as was discussed in a specific note (Bogey *et al.* 2011*c*), to the spectral shapes encountered for turbulent wall-bounded flows because of the presence of large-scale elongated structures. As the boundary-layer profile changes from laminar to turbulent, the magnitude of the low-frequency components at $St_D < 0.8$ slightly strengthens in figure 4(*a*), which may be linked to the larger 99 % velocity thickness of the profile. Most obviously, the dominant components in figure 4(*b*) shift towards higher modes, resulting in peaks at $n_\theta = 50$ for jetBL, $n_\theta = 51$ for jetT1 and $n_\theta = 64$ for jetT2, as reported in table 5. The turbulent structures are thus spaced out by $\lambda_\theta = 0.13r_0$, $\lambda_\theta = 0.12r_0$ and $\lambda_\theta = 0.10r_0$, respectively. The modification of their spatial arrangement in the azimuthal direction may be related to the increase of the velocity gradient.

The spectra evaluated in the outer boundary-layer region at $r = r_0 - \delta_{94} = 0.827r_0$ in all cases are depicted in figure 5. Their levels are normalized by the r.m.s. values of velocity fluctuations at this position, equal to $\langle u_z'^2 \rangle^{1/2} = 0.0248u_j$ for JetBL, $0.0283u_j$ for JetT1 and $0.0285u_j$ for JetT2. The spectra are very similar to each other, both in shape and in amplitude. Compared to the near-wall spectra, two important differences can be noticed. First, a significant amount of energy is contained by the components centred around a Strouhal number of $St_D = 3.2$ in figure 5(*a*), whereas a rapid collapse is observed for $St_D \geqslant 1.6$ in figure 4(*a*). Second, the dominant mode in the azimuthal direction is $n_\theta \simeq 40$ for all cases in figure 5(*b*), whereas it is higher, and increases for a lower boundary-layer shape factor in figure 4(*b*). Therefore, the turbulent structures organize differently near the wall and further away, as expected (Tomkins & Adrian 2005). Furthermore, they appear to depend on the form of the velocity profile in the first region, but not in the second one.

3.1.2. *Very near-nozzle instability waves*

In order to characterize the instability waves initially growing in the shear layers, an inviscid linear stability analysis is carried out following the methodology described in § 2.4 from the LES mean flow profiles at $z = 0.1r_0$, corresponding to $z \simeq 3.6\delta_\theta(0)$ in terms of nozzle-exit boundary-layer momentum thickness $\delta_\theta(0)$. The mean velocity profiles at this position are shown in figure 6(*a*). They are very similar to the nozzle-exit profiles of figure 2(*a*), and have momentum thicknesses only 2 % larger than the exit values reported in table 5. This persistence of the mean velocity profile is in

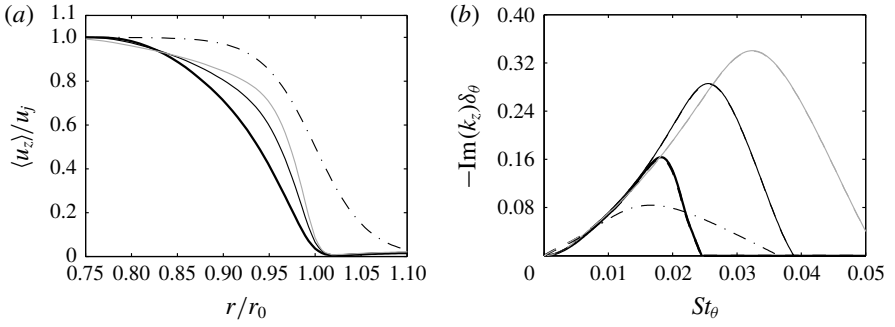

FIGURE 6. Representation (a) of the profiles of mean axial velocity $\langle u_z \rangle$ at $z = 0.1r_0$ and (b) of the instability growth rates $-\mathrm{Im}(k_z)$ obtained for the profiles using an inviscid linear stability analysis for modes $n_\theta = 0$ for ——— jetBL, —— jetT1, ——— jetT2 and $n_\theta = 1$ for – – – jetBL, −−− jetT1, – – – jetT2, as a function of St_θ; −·−· results for a two-dimensional hyperbolic–tangent velocity profile with $\delta_\theta = 0.0288r_0$.

	St_D	St_θ	St_ω	St^+
JetBL	1.21	0.018	0.071	0.078
JetT1	1.79	0.026	0.070	0.050
JetT2	2.30	0.032	0.067	0.040

TABLE 6. Peak Strouhal numbers St_D, St_θ, St_ω and St^+ of instability growth rates obtained using an inviscid linear stability analysis at $z = 0.1r_0$.

agreement with the measurements of Morris & Foss (2003) downstream of a sharp corner for a turbulent boundary layer at $Re_\theta = 4650$, as indicated in table 1. For the comparison, a hyperbolic–tangent velocity profile with $\delta_\theta = 0.0288r_0$, that is the momentum thickness imposed at the pipe-nozzle inlet, is also plotted. This type of analytical profile is often used in linear stability analyses for mixing layers and jets (Michalke 1984), providing good predictions of the peak Strouhal number St_θ for initially laminar conditions (Gutmark & Ho 1983), but poor ones for initially turbulent conditions (Drubka & Nagib 1981; Hussain & Zaman 1985).

The instability amplification rates $-\mathrm{Im}(k_z)\delta_\theta$ computed for the first two azimuthal modes $n_\theta = 0$ and $n_\theta = 1$ are represented in figure 6(b) as a function of the Strouhal number St_θ. Their peak frequencies are gathered in table 6. The curves obtained for the two modes are superimposed, due to the value of $\delta_\theta/r_0 < 1/25$ (Michalke 1984), with a slight predominance of the axisymmetric mode. Their sensitivity to the velocity profile is much more spectacular. For jetBL, the range of unstable frequencies is narrower and the peak growth rate is higher than those for the hyperbolic–tangent profile. Despite these discrepancies, the peak grow rates are reached at very similar Strouhal numbers, namely $St_\theta = 0.018$ for jetBL and $St_\theta = 0.017$ for the analytical profile. For the two other jets, the range of unstable frequencies broadens and the growth rates strengthen as the exit profile deviates from a laminar profile. In addition, the peak Strouhal number increases to $St_\theta = 0.026$ for jetT1 and to $St_\theta = 0.032$ for jetT2.

The present changes in peak frequency at $z = 0.1r_0 \simeq 3.6\delta_\theta(0)$ depending on the boundary-layer profile are consistent with the data of the literature. For instance, the peak Strouhal numbers of $St_\theta = 0.022 - 0.028$ measured by Drubka & Nagib

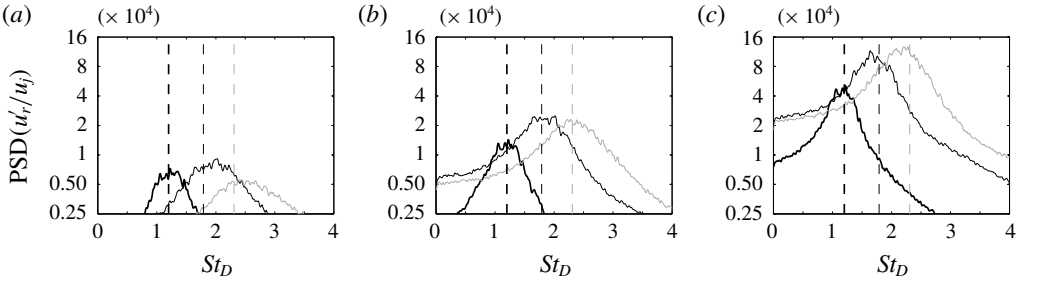

FIGURE 7. Power spectral densities of radial velocity fluctuations u_r' at $r = r_0$ at (*a*) $z = 0.1r_0$, (*b*) $z = 0.2r_0$ and (*c*) $z = 0.4r_0$, as a function of St_D: ——— jetBL, —— jetT1, ——— jetT2; and peak frequencies of instability growth rates obtained using an inviscid linear stability analysis at $z = 0.1r_0$: – – – jetBL, – – – jetT1, – – – jetT2.

(1981) and Hussain & Zaman (1985) in initially turbulent mixing layers are greater than those found around $St_\theta = 0.013$ in initially laminar mixing layers. Closer to this study, in the experiments of Morris & Foss (2003), a hump emerges at $St_\theta \simeq 0.06$ in the velocity spectrum acquired $3.54\delta_\theta(0)$ downstream of a sharp edge, where $\delta_\theta(0)$ here denotes the boundary-layer momentum thickness at the edge. Finally, the linear stability analyses performed at $z = 0.08r_0$ in Fontaine *et al.* (2015) and at $z = 0.16r_0$ in Brès *et al.* (2018) for the jets reported in table 1 also reveal peak amplification rates at higher St_θ for turbulent than for laminar nozzle-exit flow conditions. Indeed, while the peak Strouhal numbers emerge at $St_\theta = 0.012$–0.014 for the short-nozzle case in Fontaine *et al.* (2015) and for Baseline_LES_10M in Brès *et al.* (2018), they are equal to $St_\theta = 0.09$ for the long-nozzle case and to $St_\theta = 0.024$ for BL16M_WM_Turb. Remark that the positions of $z = 0.08r_0$ for the long-nozzle case and of $z = 0.16r_0$ for BL16M_WM_Turb correspond respectively to $z = 1.9\delta_\theta(0)$ and to $z = 11\delta_\theta(0)$. The variations of the peak frequencies with the axial position will be discussed later in § 3.2.3.

Instead of the momentum thickness, the peak frequency of the instability growth rates can be related to other length scales of the velocity profiles, such as the vorticity thickness δ_ω or viscous wall units at the nozzle exit, as proposed by Morris & Foss (2003). The resulting Strouhal numbers $St_\omega = f\delta_\omega/u_j$ and $St^+ = f\nu/u_\tau^2$ are given in table 6. As the boundary-layer shape factor H decreases, the latter varies from 0.078 for jetBL down to 0.040 for jetT2, whereas the former remains very close to 0.07. Therefore, the frequency of the initial instability wave is primarily linked to the high-shear portion of the velocity profiles, as was noted by Fontaine *et al.* (2015).

The spectra of radial velocity fluctuations calculated at $r = r_0$ at $z = 0.1r_0$, $z = 0.2r_0$ and $z = 0.4r_0$ are represented in figure 7 as a function of St_D. The peak diameter-based Strouhal numbers obtained from the mean-flow profiles at $z = 0.1r_0$ using the linear stability analysis, provided in table 6, are also indicated. For all jets, a hump appears in the spectra, centred on a frequency moving slowly towards lower frequencies in the downstream direction, as for the separating boundary layer of Morris & Foss (2003). The peak frequencies are in very good agreement with the linear stability results, especially in figure 7(*b*) for $z = 0.2r_0$. Moreover, the hump rapidly grows, at a rate which is lowest for jetBL and highest for jetT2, as predicted by the instability amplification rates of figure 6(*b*). Therefore, for the present initially disturbed jets, the flow development very near the nozzle is driven by the instability waves examined in this section.

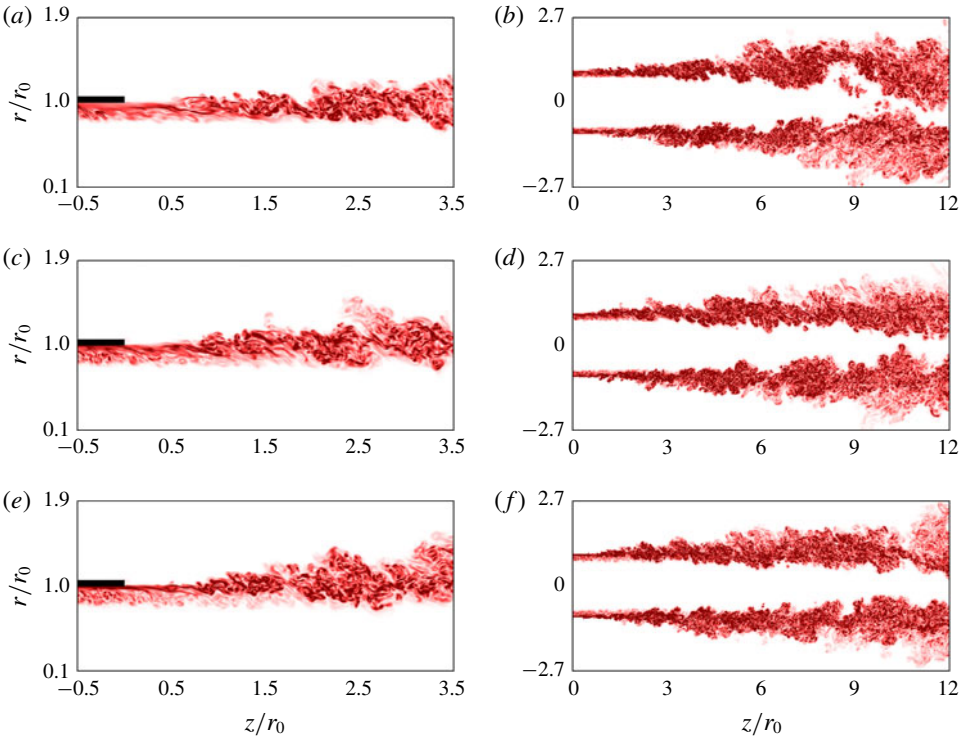

FIGURE 8. (Colour online) Snapshots in the (z, r) plane of vorticity norm $|\boldsymbol{\omega}|$ for (a) jetBL, (b) jetT1 and (c) jetT2. The colour scales range from 0 up to (a,c,e) $18u_j/r_0$ and (b,d,f) $9u_j/r_0$, from white to red.

3.2. *Shear-layer development*

3.2.1. *Vorticity snapshots*

Instantaneous fields of vorticity norm obtained down to $z = 3.5r_0$ and to $z = 12r_0$ are represented in figures 8(a,c,e) and 8(b,d,f), respectively. Very near the nozzle lip, in figure 8(a,c,e), the levels of vorticity are higher for jetT2 than for the two other jets due to the sharper boundary-layer profile. In that region, the turbulent structures are elongated in the downstream direction, which is characteristic of wall-bounded flows. In the radial direction, their length scales are of the order of boundary-layer thickness for jetBL, but are much smaller for jetT1 and especially for jetT2. For the latter jet, in particular, strong levels of vorticity are only found around $r = r_0$. This is the case nearly down to $z = 0.5r_0$, in agreement with the persistence of the mean boundary-layer profile mentioned above. These results supports again that the initial shear-layer development is essentially related to the vorticity thickness of the velocity profile. Further away from the nozzle, the shear layers seem to roll up around $z = 1.5r_0$ for jetBL but earlier for jetT1 and jetT2, which is in line with the instability amplification rates of the previous section. Then, they exhibit typical features of turbulent mixing layers. Finally, in figure 8(b,d,f), the mixing layers appear to be fully developed for $z \gtrsim 4r_0$. However, they spread faster for jetBL than for the two other jets. The presence of large-scale structures resembling the coherent structures of the flow visualizations of Brown & Roshko (1974) is also more obvious for the laminar boundary-layer profile than for the non-laminar profiles. Similar

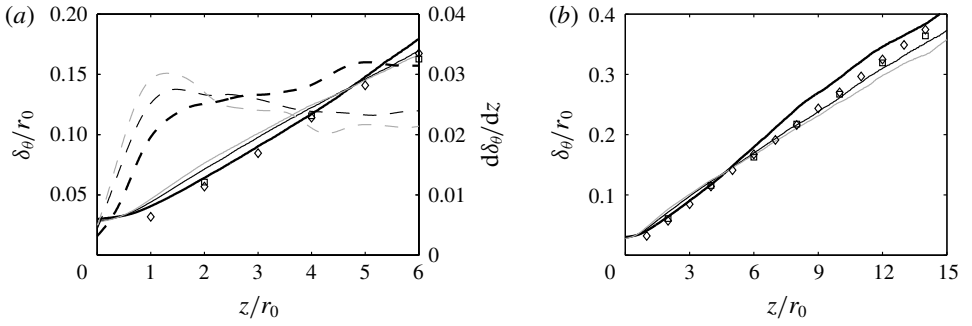

FIGURE 9. Variations of shear-layer momentum thickness δ_θ for ——— jetBL, —— jetT1 and ——— jetT2 and of spreading rate $d\delta_\theta/dz$ for – – – jetBL, −−− jetT1 and – – – jetT2; measurements for isothermal jets at $M = 0.9$: ◇ Fleury (2006) at $Re_D = 7.7 \times 10^5$ and □ Castelain (2006) at $Re_D = 10^6$.

effects of the exit velocity profile on the organized structures in the shear layers of jets were recently revealed by the experiments of Zaman (2017) using the ASME and the conical nozzles. It should be reminded that the definition of coherent structures may vary from one researcher to another. In this work, following Hussain (1986) and Fieldler (1988), they refer to regions of correlated and concentrated vorticity, of size comparable to the transverse length scale of the shear layer, which are spatially isolated from each other and show similarity with the corresponding structures of the (preceding) laminar–turbulent transition.

3.2.2. *Flow field properties*

The variations of the shear-layer momentum thickness are represented over $0 \leqslant z \leqslant 6r_0$ in figure 9(*a*) and over $0 \leqslant z \leqslant 15r_0$ in figure 9(*b*). The spreading rates $d\delta_\theta/dz$ are also shown in figure 9(*a*). The differences are significant between jetBL and jetT1 with boundary-layer profiles with $H = 2.29$ and 1.96, but they are rather weak between the two transitional cases with $H = 1.96$ and 1.71. For $z \leqslant 3r_0$, the mixing layers develop faster for jetT1 and jetT2 than for jetBL. This can be due to the higher growth rates of the jet initial instability waves as the shape factor H decreases, highlighted in figure 6. Farther downstream, in contrast, the mixing layers spread most rapidly for jetBL, which was suggested by the vorticity fields of figure 8, but has no evident cause at first sight. In this region, a better agreement with the measurements of Fleury (2006) and Castelain (2006) for jets at $M = 0.9$ and $Re_D \simeq 10^6$, undoubtedly initially turbulent, is obtained for the jets with non-laminar boundary-layer profiles. Furthermore, for jetBL, the shear-layer spreading rate increases monotonically with the axial distance up to values around 0.030 at $z = 5r_0$. For jetT1 and jetT2, on the contrary, they reach peak values of 0.0275 at $z = 1.3r_0$ and of 0.030 at $z = 1.5r_0$, respectively, and do not exceed values of 0.024 for $z \geqslant 4r_0$.

In order to illustrate the change of the mean-flow profiles in the region of boundary-layer/mixing-layer transition, the profiles of mean axial velocity at $z = 0.8r_0$, $1.6r_0$ and $3.2r_0$ are provided in figure 10. The radial distances are normalized by the local shear-layer momentum thicknesses, which, however, are nearly the same in the present jets at $z = 0.8r_0$ and $3.2r_0$, and only vary from $0.054r_0$ in jetBL up to $0.065r_0$ in jetT2 at $z = 1.6r_0$. At $z = 0.8r_0$, corresponding to $z = 28\delta_\theta(0)$, the velocity profiles

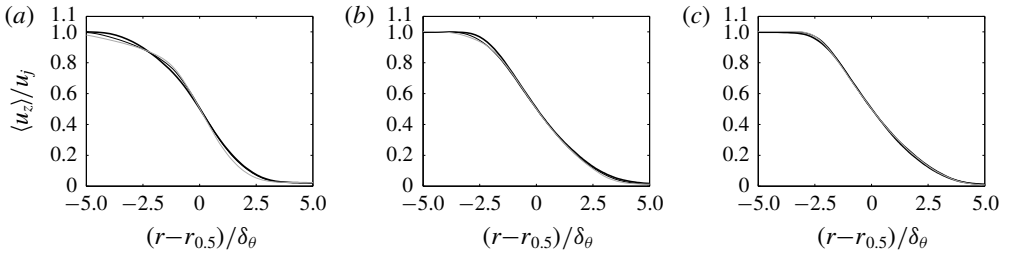

FIGURE 10. Radial profiles of mean axial velocity $\langle u_z\rangle$ at (*a*) $z=0.8r_0$, (*b*) $z=1.6r_0$ and (*c*) $z=3.2r_0$: ——— jetBL, —— jetT1, ——— jetT2.

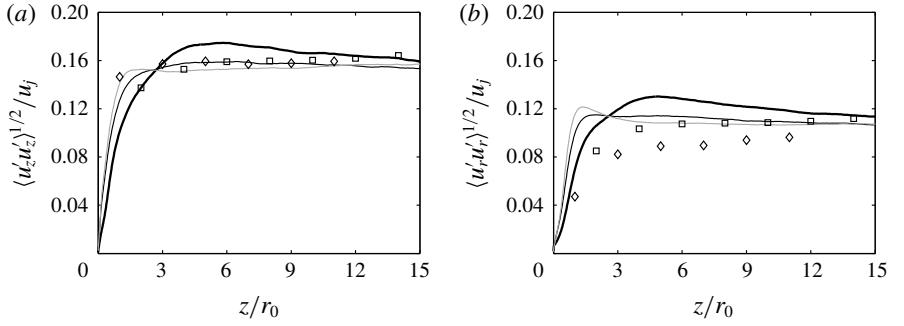

FIGURE 11. Variations of the r.m.s. values of (*a*) axial and (*b*) radial velocity fluctuations u_z' and u_r' at $r=r_0$: ——— jetBL, —— jetT1, ——— jetT2; peak values measured in isothermal jets at $M=0.9$: ◇ Fleury (2006) at $Re_D=7.7\times10^5$ and □ Castelain (2006) at $Re_D=10^6$.

	$\langle u_z'^2\rangle^{1/2}/u_j$ (%)	$\langle u_r'^2\rangle^{1/2}/u_j$ (%)	$\langle u_\theta'^2\rangle^{1/2}/u_j$ (%)	$\langle u_r'u_z'\rangle^{1/2}/u_j$ (%)
JetBL	17.4	13.1	14.5	10.6
JetT1	15.9	11.7	13.5	9.6
JetT2	15.5	12.3	14.0	9.9

TABLE 7. Peak turbulence intensities in the jets.

differ significantly. This is particularly the case for their high-speed portions, which still bear strong similarities with the nozzle-exit profiles. The latter result is consistent with that obtained for a turbulent boundary layer at $z=29\delta_\theta(0)$ in the experiments of Morris & Foss (2003). Farther away from the nozzle, the mean velocity profiles are very close to each other at $z=1.6r_0$ and almost superimposed at $z=3.2r_0$, and exhibit no clear reminiscence of the boundary-layer profiles.

The r.m.s. values of axial and radial velocity fluctuations at $r=r_0$ are displayed down to $z=15r_0$ in figure 11. They follow trends which are similar to those for the mixing-layer spreading rate. Just downstream of the nozzle, they increase more rapidly for jetT1 and jetT2 than for jetBL, thus reaching peaks around $z=r_0$ in the former case, but $z=5r_0$ in the latter. In addition, the levels are lower for the transitional boundary-layer profiles. This is true for the peak levels in the jets, given in table 7, which are equal, for u_z' and u_r' for instance, to approximately $0.157u_j$ and $0.12u_j$ for

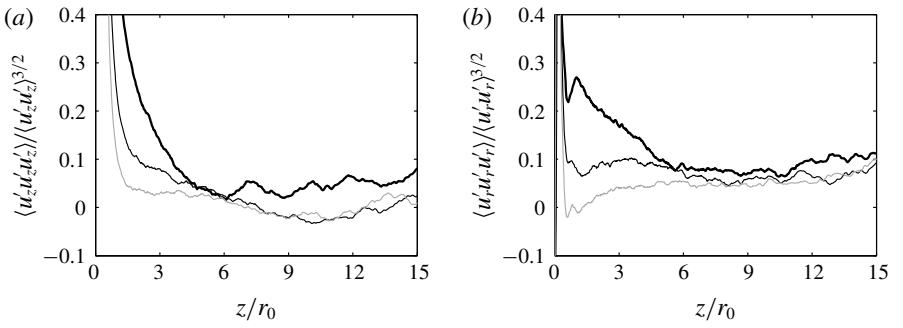

FIGURE 12. Variations of the skewness values of (*a*) axial and (*b*) radial velocity fluctuations u_z' and u_r' at $r = r_0$: ——— jetBL, —— jetT1, ——— jetT2.

jetT1 and jetT2, but to $0.174u_j$ and $0.131u_j$ for jetBL. The difference in turbulence intensity is also significant down to $z = 15r_0$, which is roughly the position of the end of the jet potential core. Therefore, the effects of the exit boundary-layer profile on the turbulence in the mixing layers last far downstream of the nozzle, despite, notably, the nearly identical mean-flow profiles obtained at $z = 3.2r_0$ in figure 10(*c*). Finally, as for the shear-layer momentum thickness, the results for the jets with non-laminar mean velocity profiles better agree with the measurements of Fleury (2006) and Castelain (2006) than those for jetBL.

Comparisons between numerical and experimental data may only be fully relevant for identical upstream flow conditions. It can however be mentioned that in the similarity region of an axisymmetric mixing layer, initially with $Re_\theta = 349$, $u_e'/u_j = 6.18\,\%$ and $H = 2.47$, Hussain & Zedan (1978*b*) obtained a spreading rate of 0.0294 and a peak axial turbulence intensity of 16.7 %, which are both comparable to the values reached in jetBL. Moreover, the changes undergone by the mixing layers of the present jets as the nozzle-exit velocity profile deviates from a laminar profile, namely a slower growth and weaker velocity fluctuations, correspond to those observed experimentally when initially laminar shear layers are tripped and become initially turbulent (Hill *et al.* 1976; Browand & Latigo 1979; Husain & Hussain 1979). They also resemble the changes induced by increasing the exit turbulence levels only (Hussain & Zedan 1978*a*; Bogey *et al.* 2012*b*).

Finally, the skewness factors of the axial and radial velocity fluctuations at $r = r_0$ are represented in figure 12. In the vicinity of the nozzle exit, in all cases, they differ appreciably from zero, which is expected at the interface between the highly disturbed shear layers and the ambient medium. Their positive values are due to the sudden eruptions of high-velocity fluid at the outer edge of the mixing layers. For jetT1 and jetT2, the skewness factors rapidly decrease, whereas they remain greater than 0.1 down to $z = 4r_0$ for jetBL. This can be related to the slower initial development of the shear layers in the latter case. Farther downstream, for $z \geqslant 6r_0$, the skewness factors, albeit much lower than previously, are still higher for jetBL than for the other jets. Given the links between velocity skewness and large-scale vortices in free shear flows (Yule 1978), this result suggests the presence of stronger coherent structures in the first jet.

3.2.3. *Instability waves and velocity spectra*

Some results of the inviscid linear stability analysis carried out, as reported in § 2.4, from the LES mean-flow fields between $z = 0.02r_0$ and $5r_0$ are provided in order to

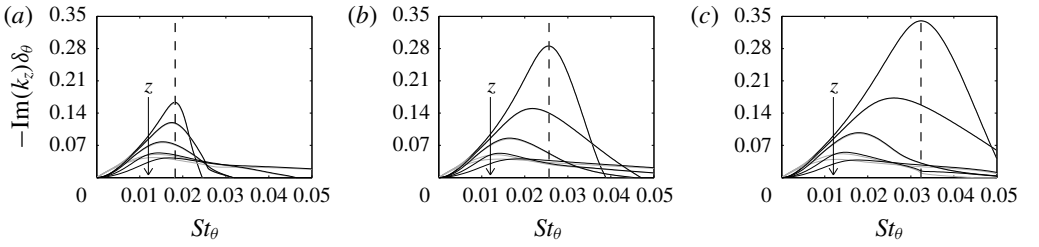

FIGURE 13. Representation of the instability growth rates $-\mathrm{Im}(k_z)$ obtained using an inviscid linear stability analysis at $z = 0.1r_0$, $0.4r_0$, $0.8r_0$, $1.6r_0$ and $3.2r_0$ for —— $n_\theta = 0$ and —— $n_\theta = 1$ for (*a*) jetBL, (*b*) jetT1 and (*c*) jetT2, as a function of St_θ; – – – peak frequencies at $z = 0.1r_0$.

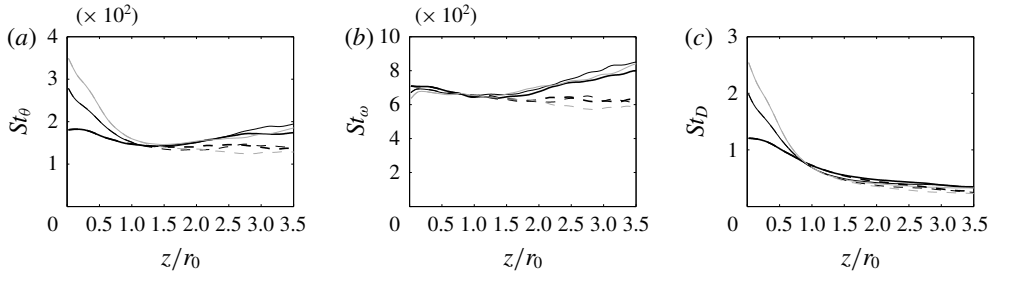

FIGURE 14. Axial variations of the peak Strouhal numbers (*a*) St_θ, (*b*) St_ω and (*c*) St_D of instability growth rates obtained for —— jetBL, —— jetT1, —— jetT2 for n_θ=0; – – –, – – –, – – – corresponding results for $n_\theta = 1$.

investigate the properties of the instability waves, and their variations in the axial direction, during the boundary-layer/mixing-layer transition and further downstream, They will help us to identify the possible cause of the differences between the shear-layer developments.

The instability amplification rates $-\mathrm{Im}(k_z)\delta_\theta$ calculated for $n_\theta = 0$ and $= 1$ at $z = 0.1r_0$, $0.4r_0$, $0.8r_0$, $1.6r_0$ and $3.2r_0$ are represented in figure 13 as a function of the Strouhal number St_θ. The curves obtained for the two azimuthal modes are nearly superimposed on each other except for $z = 3.2r_0$, where lower unstable frequencies are found for $n_\theta = 1$ than for $n_\theta = 0$ due to the mixing-layer thickness of $\delta_\theta \simeq 0.1r_0$ at this location (Michalke 1984). As the distance from the nozzle exit increases, the amplification curves change appreciably in level and shape for all jets. For jetBL, the instability growth rates are lower, and the ranges of unstable frequencies broaden. However, the peak Strouhal numbers, equal to $St_\theta = 0.018$ at $z = 0.1r_0$, do not vary much with the axial position. For jetT1 and jetT2 with non-laminar boundary-layer profiles, the changes with the distance from the nozzle are more important. The reduction of the growth rates is stronger and, above all, the peak Strouhal numbers St_θ, of 0.026 for jetT1 and of 0.032 for jetT2 at $z = 0.1r_0$, decrease significantly. At $z = 3.2r_0$, finally, the amplification curves are the nearly the same for the three jets, which is not surprising given the very similar velocity profiles of figure 10(*c*).

In order to highlight their variations downstream of the nozzle, the peak Strouhal numbers St_θ of the instability growth rates are plotted in figure 14(*a*) between $z = 0.02r_0$ and $3.5r_0$. The values obtained for $n_\theta = 0$ and 1 are identical to each other

down to $z \simeq r_0$, and then gradually diverge due to the thickening of the mixing layer, yielding $St_\theta \simeq 0.018$ for $n_\theta = 0$ and $St_\theta \simeq 0.014$ for $n_\theta = 1$ at $z = 3.5r_0$ in all cases. More interestingly, strong discrepancies appear in the vicinity of the nozzle exit between the three jets. In that region, for jetBL, the peak Strouhal numbers do not change much with the axial distance and remain close to a value of $St_\theta = 0.018$ corresponding roughly to the Strouhal numbers emerging farther downstream in the mixing layers. For jetT1 and jetT2, on the contrary, they rapidly decrease during the changeover from a boundary-layer profile to a mixing-layer profile, from values of the order of or higher than 0.03 at $z = 0.02r_0$ down to values lower than 0.02 at $z \simeq 0.6r_0 \simeq 20\delta_\theta(0)$. These variations of St_θ are in very good agreement with the experimental data of Morris & Foss (2003) for a turbulent boundary layer.

As in the study mentioned above, a scaling with the local shear-layer vorticity thickness is applied to the peak frequencies of the instability growth rates. The resulting Strouhal numbers St_ω are shown in figure 14(*b*) between $z = 0.02r_0$ and $3.5r_0$. For the present jets, they are very close to each other at any of the locations considered. This is particularly true, despite the different boundary-layer profiles, near the nozzle, where Strouhal numbers $St_\omega \simeq 0.07$ are continuously found between $z = 0.02r_0$ and $z \simeq 2r_0$. Therefore, for a given mean flow profile, the peak frequency of the instability waves is only fixed by the maximum velocity gradient.

The variations of the most unstable Strouhal numbers St_θ downstream of the nozzle do not reflect those of the most unstable frequencies because of the increase of the shear-layer momentum thickness in the axial direction. For that reason, the instability growth rates $-\mathrm{Im}(k_z)r_0$ obtained for $n_\theta = 0$ and 1 at $z = 0.4r_0$, $0.8r_0$, $1.6r_0$ and $3.2r_0$ are re-plotted in figure 15 as a function of the diameter-based Strouhal number St_D. The peak Strouhal numbers St_D are also represented in figure 14(*c*) between $z = 0.02r_0$ and $z = 3.5r_0$. As the distance from the nozzle increases, they move to lower values due to the shear-layer thickening. During the initial stage of flow development between the nozzle exit and $z \simeq 0.6r_0$, the frequency decrease is however much more pronounced for jetT1 and jetT2 than for jetBL. In their linear stability analyses, Brès *et al.* (2018) recently noted, as in this work, that downstream of the nozzle the range of the unstable frequencies are more quickly reduced for their initially turbulent jet than for their initially laminar jet with thicker exit boundary layer. They attributed this to the fact that the instability waves in the near-nozzle region grow at a higher rate in the first jet because of the faster shear-layer spreading in this case. On the basis of the present results, this appears to be also strongly linked to the difference in peak instability frequency between laminar and non-laminar boundary-layer profiles.

The dependence of the range of the unstable frequencies on the boundary-layer profiles has substantial effects on the spatial evolution of the instability waves developing downstream of the nozzle. Examine, for instance, the peak frequencies obtained at $z = 0.1r_0$ in figure 15. The more non-laminar the boundary-layer profile, the earlier they leave the range of the unstable frequencies. The growth rates calculated between $z = 0.02r_0$ and $3.5r_0$ for the peak frequencies at $z = 0.1r_0$, $0.2r_0$ and $0.4r_0$, chosen to cover the frequency range of the initial instability waves, are also represented in figure 16. In all cases, they sharply decrease downstream of the nozzle. However, they remain appreciable down to $z \simeq 3.5r_0 \simeq 125\delta_\theta(0)$ in figure 16(*a*) for jetBL, whereas they become negligible or negative as early as $z \simeq r_0 \simeq 35\delta_\theta(0)$ in figure 16(*b*,*c*) for jetT1 and jetT2. As a result, the instability waves developing very near the nozzle continue to be amplified, even at a low rate, over a relatively large axial distance for the laminar boundary-layer profile, whereas they are rapidly damped for the non-laminar profiles.

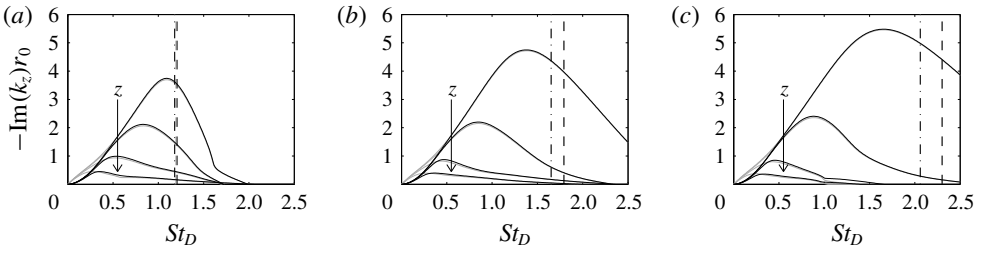

FIGURE 15. Representation of —— the instability growth rates $-\mathrm{Im}(k_z)$ at $z=0.4r_0$, $0.8r_0$, $1.6r_0$ and $3.2r_0$ as a function of St_D and of the peak frequencies at – – – z=$0.1r_0$ and – · – · $0.2r_0$ obtained using an inviscid linear stability analysis for $n_\theta=0$ for (*a*) jetBL, (*b*) jetT1 and (*c*) jetT2; ———, – – – and – · – · corresponding results for $n_\theta=1$.

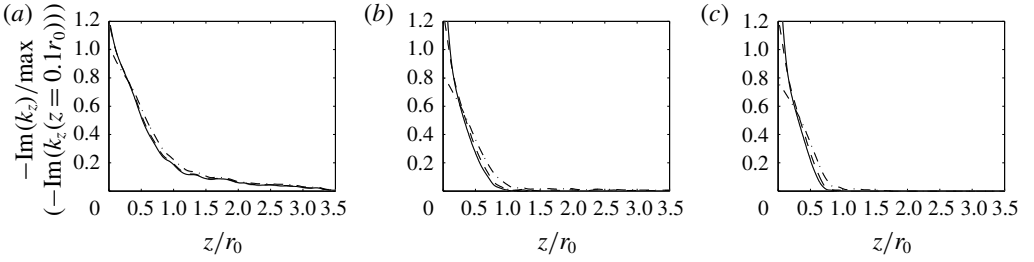

FIGURE 16. Axial variations of the instability growth rates $-\mathrm{Im}(k_z)$ obtained at the peak Strouhal numbers St_D at —— $z=0.1r_0$, – – – $z=0.2r_0$ and – · – · $z=0.4r_0$ for $n_\theta=0$ for (*a*) jetBL, (*b*) jetT1 and (*c*) jetT2, normalized by the maximum growth rates at $z=0.1r_0$; ———, – – – and – · – · corresponding results for $n_\theta=1$.

Velocity spectra computed in the mixing layers are discussed in light of the results of the linear stability analysis. First, the spectra of radial velocity fluctuations obtained at $r=r_0$ at $z=0.8r_0$, $1.6r_0$, $3.2r_0$, $4.8r_0$, $6.4r_0$ and $10r_0$ are represented in figure 17 as a function of the Strouhal number St_D, along with the peak frequencies of instability growth rates at $z=0.1r_0$. At $z=0.8r_0$, in figure 17(*a*), the spectra resemble those of figure 7 acquired farther upstream. They are dominated by humps associated with the initial instability waves, peaking at frequencies slightly lower than those predicted at $z=0.1r_0$ due to the shear-layer thickening. As the distance from the nozzle increases, in all cases, the humps diminish and eventually vanish as turbulence develops in the mixing layers. However, for jetBL, the hump remains noticeable at $z=4.8r_0$ in figure 17(*d*), whereas it cannot be observed at $z=3.2r_0$ in figure 17(*c*) for jetT1 and jetT2. This discrepancy can be explained by the linear stability analysis, indicating a longer persistence of the initial instability waves for the laminar boundary layer than for the transitional ones. Farther downstream, at $z=6.4r_0$ and $10r_0$ in figure 17(*e*,*f*), the spectra are all broadband, but significant differences appear at low frequencies. More precisely, the levels are higher for jetBL than for jetT1 and jetT2 at $St_D \lesssim 1$. Therefore, in the jet with a laminar boundary layer, the initial instability components last over a larger distance, but also lead to stronger large-scale structures in the mixing layers after having disappeared. These results are in line with the comments on coherent structures made previously from the vorticity fields and the skewness factors at $r=r_0$, and with the visualizations of Zaman (2017) for initially nominally laminar jets.

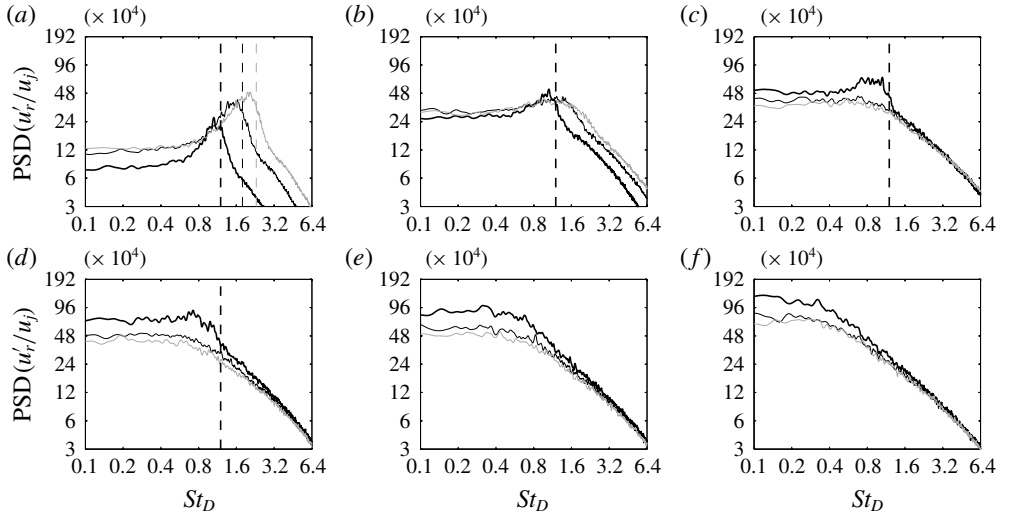

FIGURE 17. Power spectral densities of radial velocity fluctuations u_r' at $r = r_0$ at (*a*) $z = 0.8r_0$, (*b*) $z = 1.6r_0$, (*c*) $z = 3.2r_0$, (*d*) $z = 4.8r_0$, (*e*) $z = 6.4r_0$ and (*f*) $z = 10r_0$ as a function of St_D: ——— jetBL, ——jetT1, ——— jetT2; peak frequencies of instability growth rates obtained using an inviscid linear stability analysis at $z = 0.1r_0$:– – – jetBL, −−− jetT1, – – – jetT2.

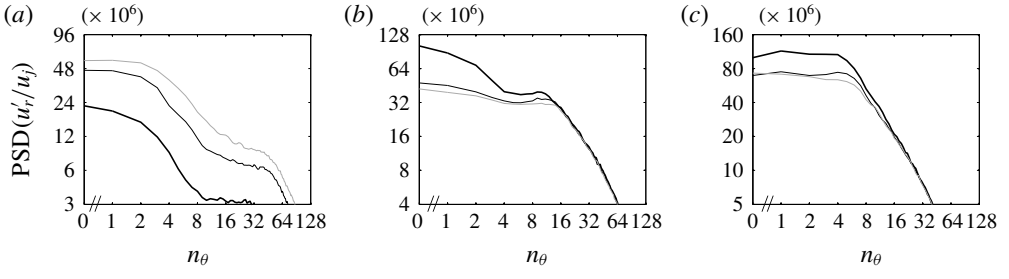

FIGURE 18. Power spectral densities of radial velocity fluctuations u_r' at $r = r_0$ at (*a*) $z = 0.8r_0$, (*b*) $z = 3.2r_0$ and (*c*) $z = 10r_0$, as a function of mode n_θ: ——— jetBL, —— jetT1, ——— jetT2.

In order to explore the azimuthal distribution of the flow disturbances, the spectra of radial velocity fluctuations at $r = r_0$ at $z = 0.8r_0$, $3.2r_0$ and $10r_0$ are depicted in figure 18 as a function of mode n_θ. At the first location, in figure 18(*a*), the spectra have nearly identical shapes over the whole range of modes considered. Since the azimuthal velocity spectra at the nozzle exit are also close to each other in figures 4(*b*) and 5(*b*), the mechanisms at play between $z = 0$ and $0.8r_0$ are of the same nature in the three jets. The levels are highest for jetT2 and lowest for jetBL, and for a given jet, they are maximum for the axisymmetric mode, remain strong up to modes $n_\theta = 3$ or 4, and then sharply decrease for higher modes. These trends are consistent with the features of the instability waves initially growing in the shear layers, namely higher amplification rates for a more turbulent nozzle-exit boundary layer, and very similar rates for the first five azimuthal modes (Brès *et al.* 2018). Farther downstream,

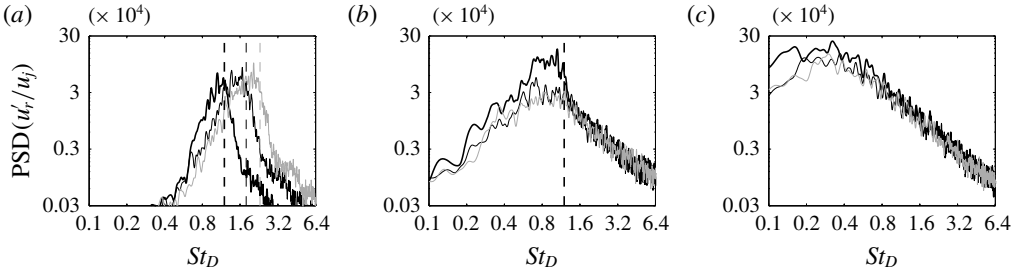

FIGURE 19. Power spectral densities for mode $n_\theta = 1$ of radial velocity fluctuations u_r' at $r = r_0$ at (*a*) $z = 0.8r_0$, (*b*) $z = 3.2r_0$ and (*c*) $z = 10r_0$, as a function of St_D: ——— jetBL, —— jetT1, ——— jetT2; peak frequencies of instability growth rates obtained using an inviscid linear stability analysis at $z = 0.1r_0$: – – – jetBL, – – – jetT1, – – – jetT2.

at $z = 3.2r_0$ and $10r_0$ in figure 18(*b*,*c*), the spectra are superimposed for $n_\theta \geqslant 16$, but the levels are higher for jetBL than for jetT1 and jetT2 at lower mode numbers. The difference in level is largest for $n_\theta \leqslant 2$ at $z = 3.2r_0$, which may be related to the presence of instability components at this position for jetBL, and for $n_\theta \leqslant 5$ at $z = 10r_0$. The intense large-scale structures in the mixing layers of jetBL revealed by the spectra of figure 17(*c*–*f*) are consequently significantly correlated in the azimuthal direction.

Finally, the spectra of radial velocity fluctuations at $r = r_0$ at $z = 0.8r_0$, $3.2r_0$ and $10r_0$ for mode $n_\theta = 1$ are displayed in figure 19 as a function of St_D. For brevity, only the results for $n_\theta = 1$ are reported, but those obtained for the other first azimuthal modes are very similar. As in figure 17(*a*,*c*,*f*), humps associated with the initial instability waves dominate at $z = 0.8r_0$, the hump still appears only for jetBL at $z = 3.2r_0$, and the low-frequency components are stronger for jetBL than for the other jets at $z = 10r_0$. The instability waves however emerge more clearly in the present case than in the spectra computed from the full velocity fields. Compared to the broadband levels, indeed, their peak levels are more than two decades higher in figure 19(*a*), whereas they are 3–4 times higher in figure 17(*a*).

3.3. *Jet development*

3.3.1. *Vorticity snapshots*

Snapshots of the vorticity norm obtained from the nozzle exit down to $z = 25r_0$ are provided in figure 20. Overall, they look like each other, and display, from upstream to downstream, the growth of the turbulent mixing layers, the closing of the jet potential cores and the regions of developed jet flows. Large-scale coherent structures may also be seen in the shear layers, for instance at $z \simeq 11r_0$ for jetBL and at $z \simeq 12r_0$ for jetT2. As the shape factor of the exit boundary-layer profile decreases, the mixing layers visibly merge later, as expected given the reduction in shear-layer spreading rate noted in previous section. As a result, the end of the potential core is located around $z = 13r_0$ in figure 20(*a*) for the laminar boundary-layer profile, but around $z = 15r_0$ in figure 20(*c*) for the transitional profile with $H = 1.71$.

3.3.2. *Flow field properties*

The variations of the centreline mean axial velocity are presented in figure 21. In figure 21(*a*), as the nozzle-exit boundary-layer profile changes from laminar

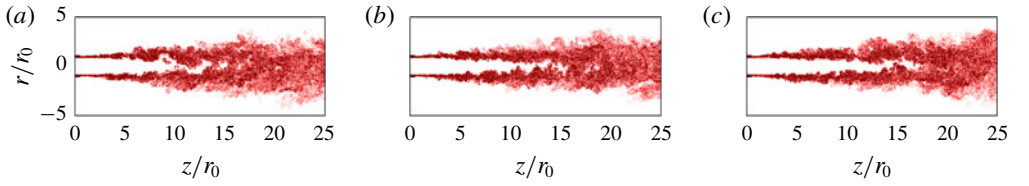

FIGURE 20. (Colour online) Snapshots in the (z, r) plane of vorticity norm $|\boldsymbol{\omega}|$ for (a) jetBL, (b) jetT1 and (c) jetT2. The colour scale ranges from 0 up to $5.5u_j/r_0$, from white to red.

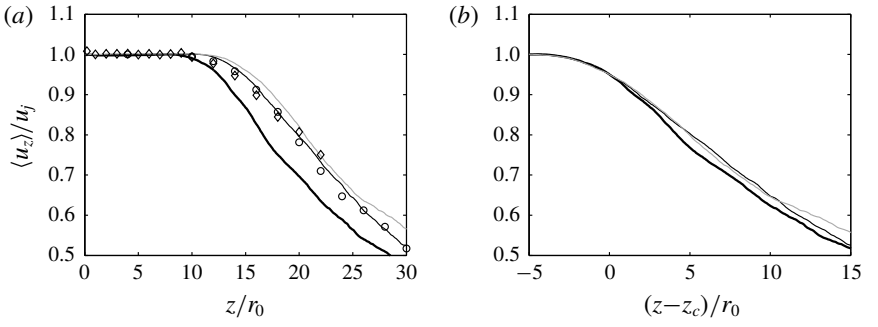

FIGURE 21. Variations of centreline mean axial velocity $\langle u_z \rangle$ as a function of (a) z and (b) $z - z_c$: ——— jetBL, —— jetT1, ——— jetT2; measurements for isothermal jets at $M = 0.9$: ∘ Lau *et al.* (1979) at $Re_D = 10^6$ and ◇ Fleury *et al.* (2008) at $Re_D = 7.7 \times 10^5$.

	z_c/r_0	$\langle u_z'^2 \rangle^{1/2}/u_j$ (%)	$\langle u_r'^2 \rangle^{1/2}/u_j$ (%)
JetBL	12.4	14.3	11
JetT1	14.8	12.9	10.1
JetT2	15.6	13.7	10.3

TABLE 8. Axial position of the end of the potential core z_c and peak r.m.s. values of velocity fluctuations u_z' and u_r' on the jet axis.

to turbulent, the jet flow develops more slowly. The potential core thus ends at $z_c = 12.4r_0$ for jetBL, $14.8r_0$ for jetT1 and $15.6r_0$ for jetT2, as indicated in table 8, where z_c is defined such as $\langle u_z \rangle(z_c) = 0.95u_j$ at $r = 0$. Even if the comparisons must be taken with care due to the moderate Reynolds number and the thick initial shear layers of the present jets, this leads to a better agreement with the measurements of Lau, Morris & Fisher (1979) and Fleury *et al.* (2008) for jets at $M = 0.9$ and $Re_D \simeq 10^6$ plotted in the figure. Downstream of the potential core, the centreline velocity seems to decay at a similar rate in three jets. According to figure 21(b), however, the decay rate is slightly lower for jetT1 and jetT2 than for jetBL.

The centreline r.m.s. values of axial velocity fluctuations are shown in figure 22(a). As for the mean-flow profiles, the differences are significant between jetBL and the two jets with transitional boundary-layer profiles, but relatively weak between the latter jets. The results are also closer to the experimental data of Lau *et al.* (1979) and Fleury *et al.* (2008) for these jets. The peak turbulence intensities are reached

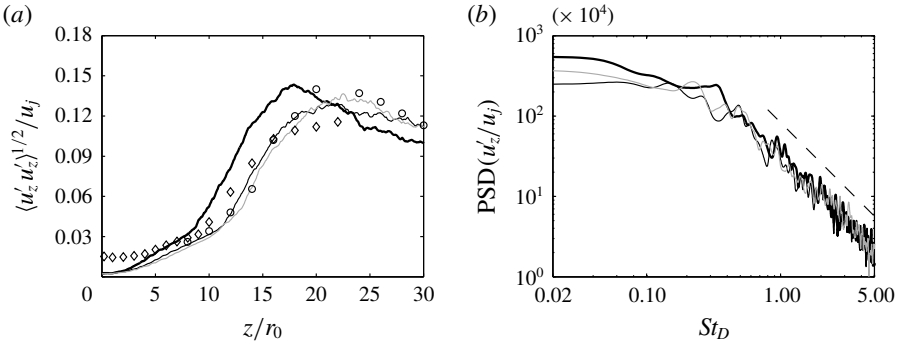

FIGURE 22. Properties of the centreline axial velocity fluctuations u_z': (*a*) axial variations of r.m.s. values and (*b*) power spectral densities at $z = z_c + 5r_0$ as a function of St_D for ——— jetBL, —— jetT1, ——— jetT2; same symbol types as in figure 21; – – – $St_D^{-5/3}$.

at $z \simeq 17r_0$ for jetBL but later at $z \simeq 22r_0$ for the two other jets, which corresponds, relative to the end of the potential core, to $z \simeq z_c + 5r_0$ and $z_c + 7r_0$ respectively. They are equal to 14.3 % for jetBL, but decrease approximately down to 13 % for the jets with non-laminar boundary-layer profiles, see also in table 8 for the radial turbulence intensities. This trend is similar to that obtained in the mixing layers down to $z = 15r_0$ in figure 11.

The spectra of the centreline axial velocity fluctuations at $z = z_c + 5r_0$, i.e. roughly at the positions of the peak r.m.s. levels, are depicted in figure 22(*b*) as a function of St_D. The spectra are superimposed and follow a $-5/3$ power law at $St_D \geqslant 0.5$, but they significantly differ and show highest levels for jetBL at lower Strouhal numbers. Therefore, stronger large-scale structures are found not only in the mixing layers, but also downstream of the potential core for the jet with a laminar boundary-layer profile. This may be the cause for the divergence in velocity decay of figure 21(*b*).

The changes observed between the present jets with laminar and transitional exit mean velocity profiles are comparable to those obtained experimentally between untripped and tripped jets (Raman *et al.* 1989, 1994; Russ & Strykowski 1993), as well as to those happening when the initial fluctuation level increases (Bogey *et al.* 2012*b*). In particular, in Raman *et al.* (1989), tripped and untripped jets at $M = 0.3$ and $Re_D = 6 \times 10^5$ with nozzle-exit turbulence intensities $u_e'/u_j \simeq 7\,\%$ and boundary-layer shape factors $H \simeq 1.55$ and 1.80, respectively, were considered. The flow development in the tripped jets is shifted by $2r_0$ in the downstream direction with respect to the untripped jet, which is in line with the results of this study. However, the peak turbulence intensities on the centreline, located at $z \simeq z_c + 7r_0$, are similar in the tripped and untripped jets, which disagrees with figure 22. The reason for this may be that the exit boundary layer of the untripped jet of Raman *et al.* (1989) is not laminar but transitional. This may also be due to the larger boundary-layer thickness in the simulations (Bogey & Marsden 2013).

3.4. *Acoustic fields*

3.4.1. *Pressure snapshots*

Snapshots of the pressure fields obtained in the LES are given in figure 23. In all cases, large-scale hydrodynamic fluctuations, classically attributed to the flow coherent

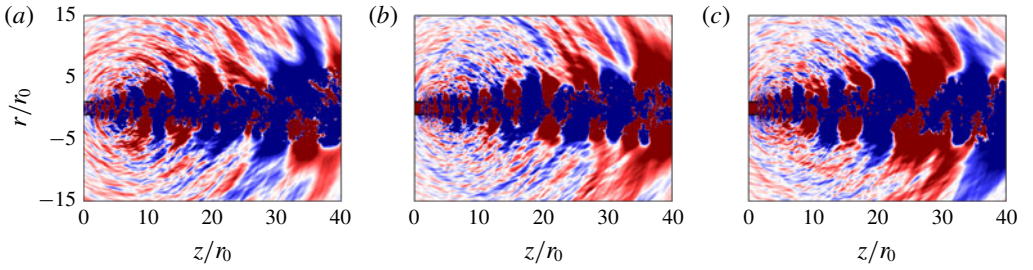

FIGURE 23. (Colour online) Snapshots in the (z, r) plane of pressure fluctuations $p - p_a$ for (*a*) jetBL, (*b*) jetT1 and (c) jetT2. The colour scale ranges from −70 to 70 Pa, from blue to red.

structures (Arndt *et al.* 1997), dominate within and very near the jets. Farther from the axis, sound waves emerge and propagate in the acoustic field. The waves emitted in the flow direction are strong and have long wavelengths, which is typical of the downstream subsonic jet noise component (Tam *et al.* 2008). Those travelling in the sideline and upstream directions are weaker and have shorter wavelengths. For the three jets, the latter ones appear to be mainly generated between $z = 5r_0$ and $10r_0$. Their amplitudes, however, are visibly higher for jetBL in figure 23(*a*) than for jetT1 and jetT2 in figure 23(*b*,*c*).

3.4.2. *Near-field and far-field pressure levels*

The properties of the jet acoustic near fields are investigated from the pressure signals recorded at $r = L_r = 15r_0$ during the LES. Those of the jet far fields are characterized from the fluctuations given at 150 radii from the nozzle exit by the two ILEE computations of sound propagation described in § 2.5. In the second case, the results presented thereafter for the angles $\phi \leqslant 60°$ relative to the jet direction are obtained in the computation in which the LES data are imposed onto the ILEE grid for $r \geqslant 7.5r_0$ at $z = L_z = 40r_0$ in order to capture most of the downstream noise components. Those for $\phi \geqslant 60°$ come from the computation in which the LES/ILEE coupling at $z = L_z$ is carried out only for $r \geqslant 14r_0$ to avoid the generation of significant spurious waves for large radiation angles where the noise levels are weak. It should be noted that the two far-field extrapolations provide nearly identical results at $\phi = 60°$ for Strouhal numbers greater than $St_D = 0.075$, demonstrating the negligible influence of the downstream extrapolation surface on the frequencies of interest. The overall sound pressure levels in this paper are all calculated by integrating the sound spectra from the Strouhal number value given above.

The noise levels obtained at $r = 15r_0$ between $z = 0$ and $40r_0$, and at 150 radii from the nozzle exit between $\phi = 15°$ and $150°$ are represented in figure 24. For illustration purposes, the experimental data of Bogey *et al.* (2007) and Bridges & Brown (2005) for isothermal jets at $M = 0.9$ and $Re_D \simeq 10^6$ are also plotted. With respect to the simulated jets, these jets have 15–20 times higher Reynolds numbers and certainly quite different nozzle-exit conditions, including much thinner exit boundary layers, which may be the cause for the extra noise radiated by the jet of Bogey *et al.* (2007) in figure 24(*a*). Despite this, however, a good qualitative agreement is found with the simulation results. More importantly, for all near-field and far-field observation points, the noise levels are 2–3 dB higher for jetBL with a laminar boundary-layer profile than for the two jets with transitional profiles. In addition, the levels for jetT2 are

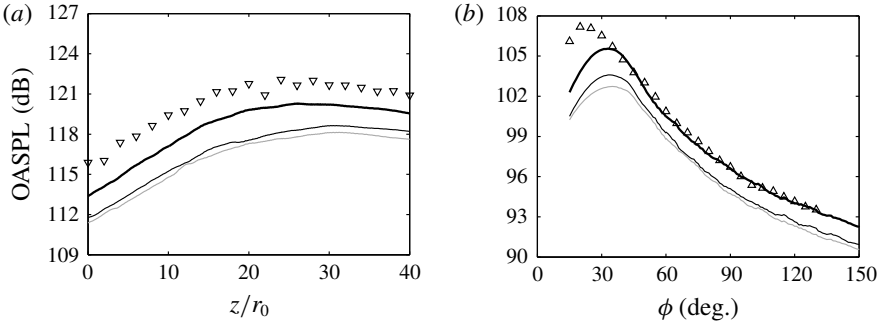

FIGURE 24. Overall sound pressure levels (OASPL) obtained (*a*) at $r = 15r_0$ and (*b*) at a distance of $150r_0$ from the nozzle exit as a function of the angle ϕ relative to the jet direction: ——— jetBL, —— jetT1, ——— jetT2; measurements for isothermal jets at $M = 0.9$: ▽ Bogey *et al.* (2007) at $Re_D = 7.9 \times 10^5$ and △ Bridges & Brown (2005) at $Re_D = 10^6$.

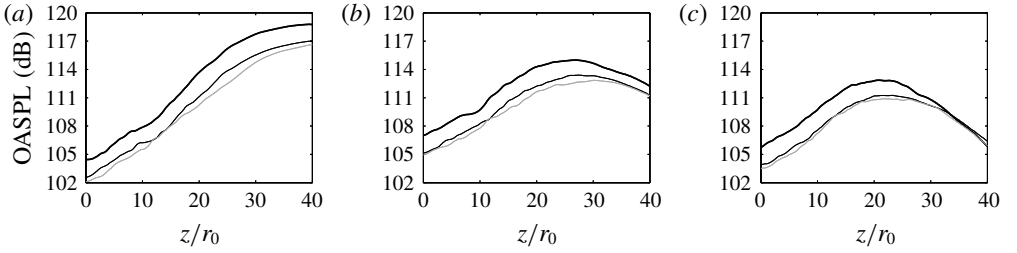

FIGURE 25. Overall sound pressure levels obtained at $r = 15r_0$ for modes (*a*) $n_\theta = 0$, (*b*) $n_\theta = 1$ and (*c*) $n_\theta = 2$:——— jetBL, —— jetT1, ——— jetT2.

just very slightly lower than those for jetT1. These trends are very similar to those reported for the r.m.s. values of velocity fluctuations in the jets, as expected due to the links existing between acoustic sources and turbulence intensities in subsonic jets (Zaman 1986).

The sound pressure levels obtained at $r = 15r_0$ for the modes $n_\theta = 0$, 1 and 2 are shown in figure 25. The levels for $n_\theta = 0$ are maximum at $z = L_z = 40r_0$ and sharply decrease in the upstream direction, whereas those for $n_\theta = 1$ and 2 reach a peak at $z \simeq 25r_0$ and $z \simeq 20r_0$, respectively. These peak positions are consistent with the far-field directivities found experimentally for the first azimuthal modes. For instance, for the jet at $M = 0.6$ of Cavalieri *et al.* (2012), noise is strongest in the downstream direction for the axisymmetric mode and for the angles of $\phi = 30°$ for $n_\theta = 1$ and of $\phi = 40°$ for $n_\theta = 2$. Here, for each mode considered, the noise levels are 2–3 dB higher for jetBL than for jetT1 and jetT2, and the levels for the last two jets do not differ appreciably, just as in figure 24 for the full pressure signals. This is in line with the resemblances of the features of the full velocity flow fields and of their first modal components in the azimuthal direction, depicted in figures 17 and 19.

The pressure spectra calculated at $r = 15r_0$ at $z = 0$, $20r_0$ and $40r_0$ are represented in figure 26 as a function of the Strouhal number St_D. Those evaluated in far field for the angles of $\phi = 30°$, 90° and 150° are provided in figure 27. When possible, the corresponding measurements of Bridges & Brown (2005) and Bogey *et al.* (2007)

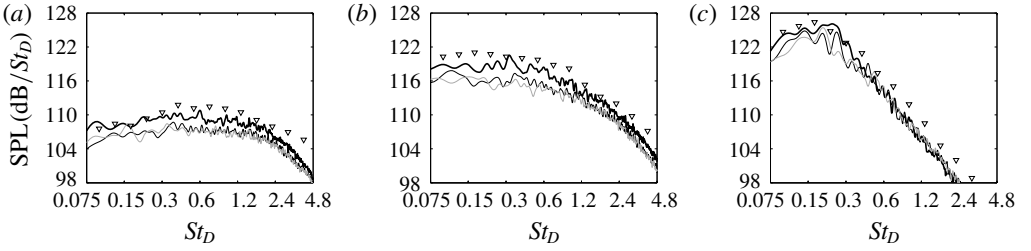

FIGURE 26. Sound pressure levels (SPL) obtained at $r = 15r_0$ at (*a*) $z = 0$, (*b*) $z = 20r_0$ and (*c*) $z = 40r_0$, as a function of St_D: ——— jetBL, —— jetT1, ——— jetT2; ▽ measurements of Bogey *et al.* (2007) for an isothermal jet at $M = 0.9$ and $Re_D = 7.9 \times 10^5$.

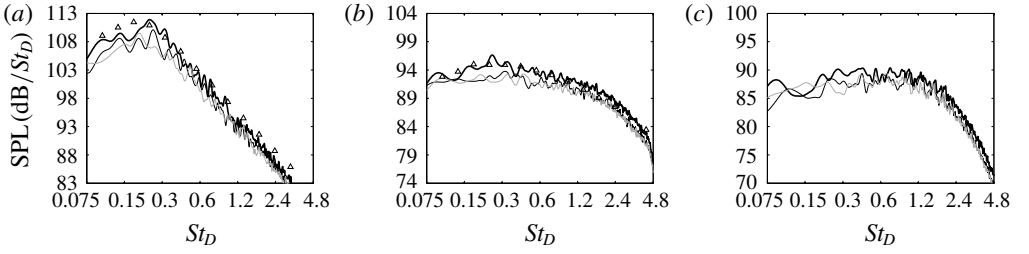

FIGURE 27. Sound pressure levels obtained at $150r_0$ from the nozzle exit for (*a*) $\phi = 30°$, (*b*) $\phi = 90°$ and (*c*) $\phi = 150°$, as a function of St_D: ——— jetBL, —— jetT1, ——— jetT2; ▽ measurements of Bridges & Brown (2005) for an isothermal jet at $M = 0.9$ and $Re_D = 10^6$.

for jets at $Re_D \simeq 10^6$ are shown. As for the overall sound levels, they compare well with the simulation results, with a better fit for the data of Bridges & Brown (2005). The spectra for the present jets have similar shapes, typical of subsonic jet noise (Mollo-Christensen, Kolpin & Martucelli 1964; Tam 1998). For small radiation angles, in figure 26(*c*) and figure 27(*a*), they are dominated by a narrow-band component centred around $St_D = 0.2$. The noise levels are 2–3 dB higher for jetBL than for the two other jets for $St_D \leqslant 0.3$, but are rather close to each other for $St_D \geqslant 0.6$. This can be related to the velocity spectra of figures 17(*f*) and 22(*b*) obtained near the end of the potential core, where the downstream acoustic components originate (Panda, Seasholtz & Elam 2005; Bogey & Bailly 2007; Tam *et al.* 2008; Bogey 2019), which also contain stronger low-frequency components for jetBL but are superimposed at high frequencies. For large radiation angles, in figures 26(*a*,*b*) and 27(*b*,*c*), the pressure spectra are broadband. In that case, the emitted sound is louder for jetBL than for jetT1 and jetT2 not only at $St_D \leqslant 0.3$ as previously, but also at higher Strouhal numbers. In particular, an increase of 1–1.5 dB is noted over $1.2 \leqslant St_D \leqslant 4.8$. This most likely results from the higher turbulence intensities in the mixing layers for jetBL, in a region where the acoustic sources have a wide range of frequencies (Chu & Kaplan 1976; Fisher, Harper-Bourne & Glegg 1977; Narayanan, Barber & Polak 2002; Lee & Bridges 2005). The difference at $St_D \geqslant 3.2$ is however rather surprising given the velocity spectra of figures 17 and 22, none of which exhibits stronger components at such Strouhal numbers for jetBL.

It is difficult to compare the present results with the experimental data available for tripped and untripped jets, because tripping usually mainly results in removing the

noise generated by the vortex pairings occurring in fully laminar jets (Zaman 1985*a*; Bridges & Hussain 1987; Bogey & Bailly 2010; Bogey *et al.* 2012*b*). Nevertheless, they bear significant similarities with the results obtained for the jets exhausting from the ASME and the conical nozzles (Viswanathan & Clark 2004; Zaman 2012; Karon & Ahuja 2013). Indeed, approximately 2 dB more noise is emitted in the first case, which was attributed by Zaman (2012) to the fact that the exit boundary layers are nominally laminar with the ASME nozzle, but turbulent with the conical nozzle. This hypothesis was further supported by Karon & Ahuja (2013) who measured lower boundary-layer shape factors for the conical nozzle and found, for instance, $H = 2.34$ in the ASME case but $H = 1.71$ in the conical case for $M = 0.4$, as indicated in table 1. The difference in noise level between the ASME and the conical nozzles is maximum at frequencies typically one decade higher than the jet noise peak frequencies, and is stronger for $\phi = 90°$ than for $\phi = 30°$. Neither of these trends are observed in this work. This may be due to the thick boundary layers in the simulations, yielding a peak Strouhal number of only $St_D = 1.20$ early on in the shear layers of jetBL. By making the boundary-layer/shear-layer transition happen over a distance of $5r_0$–$6r_0$ for jetBL, the thick exit velocity profiles also allow the effects of the boundary-layer shape on the mixing-layer turbulent structures to persist, as pointed out in § 3.3.2, down to the end of the potential core, where low-frequency sound waves are radiated in the downstream direction. Thus, it can be assumed that with a thinner boundary layer, the extra noise components for the jet with a laminar nozzle-exit mean velocity profile would emerge at higher frequencies, and would be lower for small emission angles, leading to a better agreement with the ASME case.

4. Conclusion

The influence of the nozzle-exit velocity profile has been investigated for isothermal round jets at a Mach number of $M = 0.9$ and a Reynolds number of $Re_D = 5 \times 10^4$ with a boundary-layer momentum thickness of 2.8 % of the jet radius and a peak turbulence intensity of 6 % at the exit of pipe nozzle. One jet with a laminar boundary-layer profile of shape factor $H = 2.29$ and two jets with transitional profiles with $H = 1.71$ and 1.96 are considered. The jet flow and sound fields computed for the laminar profile differ significantly from those for the two transitional profiles. The latter ones are very close to each other, suggesting that similar results would be obtained for a turbulent profile. In the non-laminar cases, the jets develop more slowly, the turbulence intensities are lower in the mixing layers but also just downstream of the jet potential core, and less noise is emitted in the acoustic field. Due to the sharper velocity gradient very near the nozzle, the initial shear-layer instability waves also grow more rapidly and at higher frequencies, in agreement with the predictions of a linear stability analysis performed from the simulation profiles. Compared to the peak unstable frequencies in a mixing layer of same momentum thickness, these frequencies are similar for the jet with a laminar boundary-layer profile, but greater for the two other ones. As a result, the initial instability waves persist over a larger distance in the laminar case, organizing the flow and leading to stronger large-scale structures downstream of the boundary-layer/mixing-layer transition, than in the non-laminar cases.

By combining high-fidelity computations of jets with well-controlled upstream conditions and linear stability analyses, this study suggests explanations for and connections between some flow and acoustic features of free shear flows and jets, which have been observed experimentally for years or even decades but whose

reasons are still unclear. This is the case for the discrepancy in frequency of the initial instability waves between initially laminar and initially turbulent conditions. The present results show that this discrepancy is due to the fact that the most unstable frequencies near the nozzle are fixed by the maximum velocity gradient and not by the boundary-layer momentum thickness. Concerning the controversial issue of the persistence of coherent structures in turbulent mixing layers, it is found that that such structures are more likely to form for a laminar boundary-layer profile than for a non-laminar profile, because of the continuity of the peak instability-wave frequencies during the changeover from a boundary-layer to a mixing-layer profile in the first case, but of their significant decrease in the other one. Thus, it becomes easier to understand why for some nozzles such as the ASME nozzle, at the exit of which the flow is highly disturbed but the mean velocity profile is laminar, intense large-scale structures appear in the mixing layers and additional noise is measured in the acoustic field.

In this paper, in order to ensure a high numerical accuracy at a reasonable computational cost, the effects of the boundary-layer velocity profile have been investigated for a jet at a Reynolds number of $Re_D = 5 \times 10^4$ with a thick boundary layer. Of course, it would be interesting to consider jets at higher Reynolds numbers with thinner boundary layers in further simulations to get closer to the conditions encountered in the laboratory-scale experiments of the literature. New experiments detailing the shear-layer turbulence properties just downstream of the nozzle for laminar and turbulent nozzle-exit velocity profiles would also be a useful complement of the present work.

Acknowledgements

This work was granted access to the HPC resources of FLMSN (Fédération Lyonnaise de Modélisation et Sciences Numériques), partner of EQUIPEX EQUIP@ MESO, and of the resources of CINES (Centre Informatique National de l'Enseignement Supérieur) and IDRIS (Institut du Développement et des Ressources en Informatique Scientifique) under the allocation 2018-2a0204 made by GENCI (Grand Equipement National de Calcul Intensif). It was performed within the framework of the Labex CeLyA of Université de Lyon, within the programme 'Investissements d'Avenir' (ANR-10-LABX-0060/ANR-16-IDEX-0005) operated by the French National Research Agency (ANR).

Appendix A

In the simulations of jetT1 and jetT2, the axial velocity profiles T1 and T2 given by equation (2.4) with $i = 1$ and 2 are imposed at the pipe-nozzle inlet at $z = -2r_0$. Considering the strong similarities between the near-wall mean-flow statistics obtained for turbulent pipe and boundary-layer flows (Monty *et al.* 2009), they have been designed to fit the experimental data provided by Schubauer & Klebanoff (1955) for a boundary layer over a flat plate in the region of laminar–turbulent flow transition at two axial positions. For the comparison, the measured profiles and the T1 and T2 profiles are represented in figure 28 as a function of the distance to the wall as in the experiment, using the boundary-layer thicknesses of $\delta_{T_1} = 0.73$ cm and $\delta_{T_2} = 1.17$ cm in equation (2.4). In both cases, a very good agreement is observed close to the wall as well as far away from it.

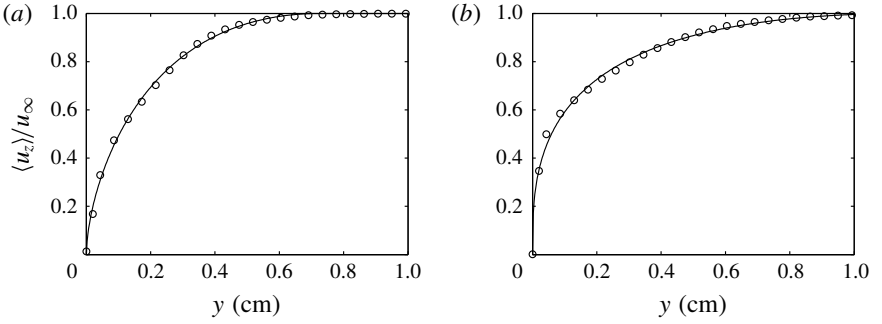

FIGURE 28. Representation of boundary-layer mean velocity profiles measured by Schubauer & Klebanoff (1955) close to the laminar–turbulent transition and of profiles given by (2.4) with $y = r_0 - r$: (*a*) ○ measurements at $x = 1.91$ m and —— profile T1 with $\delta_{T_1} = 0.73$ cm, (*b*) ○ measurements at $x = 2.06$ m and —— profile T2 with $\delta_{T_2} = 1.17$ cm.

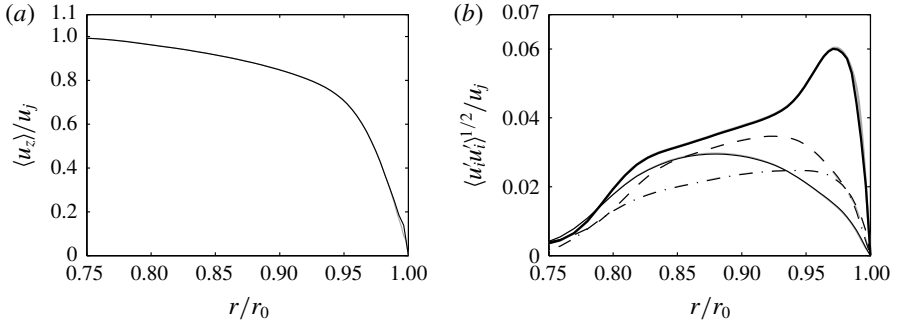

FIGURE 29. Nozzle-exit profiles (*a*) of mean axial velocity $\langle u_z\rangle$ and (*b*) of turbulence intensities ——— $\langle u_z'^2\rangle^{1/2}/u_j$, —— $\langle u_r'^2\rangle^{1/2}/u_j$, – – – $\langle u_\theta'^2\rangle^{1/2}/u_j$ and –·–· $\langle u_r'u_z'\rangle^{1/2}/u_j$ obtained for jetT2 using (black) $\Delta r/r_0 = 0.36\,\%$ and (grey) $\Delta r/r_0 = 0.18\,\%$ at $r = r_0$.

Appendix B

In a preliminary grid-sensitivity study, simulations of jetT1 and jetT2 have been performed using two grids extending in the axial direction, excluding the outflow sponge zones, only down to $z = 4r_0$ in order to save computational time. The coarsest of the two grids coincides with the grid used for the full jet LES, defined in table 3, in the boundary-layer region. The finest grid is identical to the coarsest one in the directions θ and z, but differs in the radial direction with $\Delta r/r_0 = 0.18\,\%$ instead of $\Delta r/r_0 = 0.36\,\%$ at $r = r_0$. In the two additional LES, the tripping procedure is exactly the same as in the jet LES. In the LES using the finest grid, however, the time step is twice as small because of the numerical stability condition, leading to an application of the relaxation filtering that is twice as frequent. The flow properties obtained using the two different grids at the nozzle exit are found to be nearly identical. Consequently, they depend neither on the wall-normal spacing, nor on the explicit filtering applied to remove grid-to-grid oscillations as well as to relax subgrid-scale turbulent energy.

By way of illustration, the nozzle-exit profiles of mean axial velocity and of turbulence intensities obtained for jetT2, that is for the jet with the sharpest boundary-layer profile, are represented in figure 29 using outer units and in figure 30

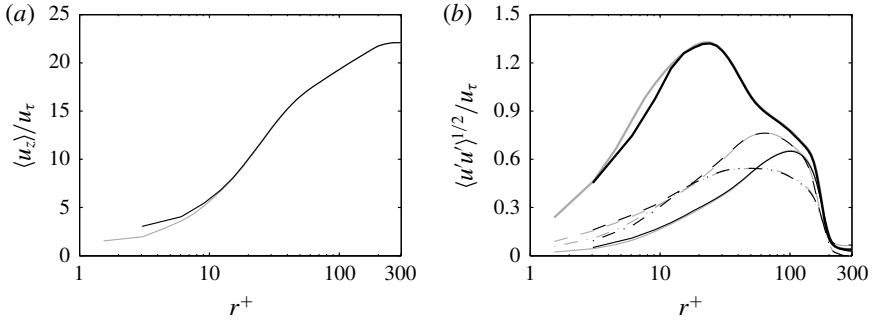

FIGURE 30. Nozzle-exit profiles (*a*) of mean axial velocity and (*b*) of turbulence intensities, represented in wall units based on the wall friction velocity using the same line types as in figure 29.

using wall units. The solutions calculated using the two grids with $\Delta r/r_0 = 0.36\,\%$ and $\Delta r/r_0 = 0.18\,\%$ at the wall superpose or are very close to each other.

REFERENCES

AHUJA, K. K., TESTER, B. J. & TANNA, H. K. 1987 Calculation of far field jet noise spectra from near field measurements with true source location. *J. Sound Vib.* **116** (3), 415–426.

ARNDT, R. E. A., LONG, D. F. & GLAUSER, M. N. 1997 The proper orthogonal decomposition of pressure fluctuations surrounding a turbulent jet. *J. Fluid Mech.* **340**, 1–33.

BERLAND, J., BOGEY, C., MARSDEN, O. & BAILLY, C. 2007 High-order, low dispersive and low dissipative explicit schemes for multi-scale and boundary problems. *J. Comput. Phys.* **224** (2), 637–662.

BOGEY, C. 2018 Grid sensitivity of flow field and noise of high-Reynolds-number jets computed by large-eddy simulation. *Intl J. Aeroacoust.* **17** (4-5), 399–424.

BOGEY, C. 2019 On noise generation in low Reynolds number temporal round jets at a Mach number of 0.9. *J. Fluid Mech.* **859**, 1022–1056.

BOGEY, C. & BAILLY, C. 2002 Three-dimensional non-reflective boundary conditions for acoustic simulations: far-field formulation and validation test cases. *Acta Acust. United Acust.* **88** (4), 463–471.

BOGEY, C. & BAILLY, C. 2004 A family of low dispersive and low dissipative explicit schemes for flow and noise computations. *J. Comput. Phys.* **194** (1), 194–214.

BOGEY, C. & BAILLY, C. 2006 Large eddy simulations of transitional round jets: influence of the Reynolds number on flow development and energy dissipation. *Phys. Fluids* **18** (6), 065101.

BOGEY, C. & BAILLY, C. 2007 An analysis of the correlations between the turbulent flow and the sound pressure field of subsonic jets. *J. Fluid Mech.* **583**, 71–97.

BOGEY, C. & BAILLY, C. 2009 Turbulence and energy budget in a self-preserving round jet: direct evaluation using large-eddy simulation. *J. Fluid Mech.* **627**, 129–160.

BOGEY, C. & BAILLY, C. 2010 Influence of nozzle-exit boundary-layer conditions on the flow and acoustic fields of initially laminar jets. *J. Fluid Mech.* **663**, 507–539.

BOGEY, C., BARRÉ, S. & BAILLY, C. 2008 Direct computation of the noise generated by subsonic jets originating from a straight pipe nozzle. *Intl J. Aeroacoust.* **7** (1), 1–22.

BOGEY, C., BARRÉ, S., FLEURY, V., BAILLY, C. & JUVÉ, D. 2007 Experimental study of the spectral properties of near-field and far-field jet noise. *Intl J. Aeroacoust.* **6** (2), 73–92.

BOGEY, C., BARRÉ, S., JUVÉ, D. & BAILLY, C. 2009*a* Simulation of a hot coaxial jet: direct noise prediction and flow-acoustics correlations. *Phys. Fluids* **21** (3), 035105.

BOGEY, C., DE CACQUERAY, N. & BAILLY, C. 2009*b* A shock-capturing methodology based on adaptative spatial filtering for high-order non-linear computations. *J. Comput. Phys.* **228** (5), 1447–1465.

BOGEY, C., DE CACQUERAY, N. & BAILLY, C. 2011*a* Finite differences for coarse azimuthal discretization and for reduction of effective resolution near origin of cylindrical flow equations. *J. Comput. Phys.* **230** (4), 1134–1146.

BOGEY, C. & MARSDEN, O. 2013 Identification of the effects of the nozzle-exit boundary-layer thickness and its corresponding Reynolds number in initially highly disturbed subsonic jets. *Phys. Fluids* **25** (5), 055106.

BOGEY, C. & MARSDEN, O. 2016 Simulations of initially highly disturbed jets with experiment-like exit boundary layers. *AIAA J.* **54** (4), 1299–1312.

BOGEY, C., MARSDEN, O. & BAILLY, C. 2011*b* Large-eddy simulation of the flow and acoustic fields of a Reynolds number 10^5 subsonic jet with tripped exit boundary layers. *Phys. Fluids* **23** (3), 035104.

BOGEY, C., MARSDEN, O. & BAILLY, C. 2011*c* On the spectra of nozzle-exit velocity disturbances in initially nominally turbulent jets. *Phys. Fluids* **23** (9), 091702.

BOGEY, C., MARSDEN, O. & BAILLY, C. 2012*a* Effects of moderate Reynolds numbers on subsonic round jets with highly disturbed nozzle-exit boundary layers. *Phys. Fluids* **24** (10), 105107.

BOGEY, C., MARSDEN, O. & BAILLY, C. 2012*b* Influence of initial turbulence level on the flow and sound fields of a subsonic jet at a diameter-based Reynolds number of 10^5. *J. Fluid Mech.* **701**, 352–385.

BRADSHAW, P. 1966 The effect of initial conditions on the development of a free shear layer. *J. Fluid Mech.* **26** (2), 225–236.

BRÈS, G. A., JORDAN, P., JAUNET, V., LE RALLIC, M., CAVALIERI, A. V. G., TOWNE, A., LELE, S. K., COLONIUS, T. & SCHMIDT, O. T. 2018 Importance of the nozzle-exit boundary-layer state in subsonic turbulent jets. *J. Fluid Mech.* **851**, 83–124.

BRIDGES, J. & BROWN, C. A. 2005 Validation of the small hot jet acoustic rig for aeroacoustics. *AIAA Paper* 2005-2846.

BRIDGES, J. E. & HUSSAIN, A. K. M. F. 1987 Roles of initial conditions and vortex pairing in jet noise. *J. Sound Vib.* **117** (2), 289–311.

BROWAND, F. K. & LATIGO, B. O. 1979 Growth of the two-dimensional mixing layer from a turbulent and nonturbulent boundary layer. *Phys. Fluids* **22** (6), 1011–1019.

BROWN, G. L. & ROSHKO, A. 1974 On density effects and large structure in turbulent mixing layers. *J. Fluid Mech.* **64** (4), 775–816.

BÜHLER, S., KLEISER, L. & BOGEY, C. 2014 Simulation of subsonic turbulent nozzle-jet flow and its near-field sound. *AIAA J.* **52** (8), 1653–1669.

CASTELAIN, T. 2006 Contrôle de jet par microjets impactants. Mesure de bruit rayonné et analyse aérodynamique. PhD thesis, Ecole Centrale de Lyon, no. 2006-33.

CASTILLO, L. & JOHANSSON, T. G. 2012 The effects of the upstream conditions on a low Reynolds number turbulent boundary layer with zero pressure gradient. *J. Turbul.* **3**, N31.

CAVALIERI, A. V. G., JORDAN, P., COLONIUS, T. & GERVAIS, Y. 2012 Axisymmetric superdirectivity in subsonic jets. *J. Fluid Mech.* **704**, 388–420.

CHANDRSUDA, C., MEHTA, R. D., WEIR, A. D. & BRADSHAW, P. 1978 Effect of free-stream turbulence on large structure in turbulent mixing layers. *J. Fluid Mech.* **85** (4), 693–704.

CHU, W. T. & KAPLAN, R. E. 1976 Use of a spherical concave reflector for jet-noise-source distribution diagnosis. *J. Acoust. Soc. Am.* **59** (6), 1268–1277.

COLES, D. E. 1962 The turbulent boundary layer in a compressible fluid. *Tech. Rep.* R-403-PR. Rand Corp.

CRIGHTON, D. G. 1981 Acoustics as a branch of fluid mechanics. *J. Fluid Mech.* **106**, 261–298.

CROW, S. C. & CHAMPAGNE, F. H. 1971 Orderly structure in jet turbulence. *J. Fluid Mech.* **48**, 547–591.

DE CHANT, L. J. 2005 The venerable 1/7th power law turbulent velocity profile: a classical nonlinear boundary value problem solution and its relationship to stochastic processes. *Appl. Maths Comput.* **161** (2), 463–474.

DRUBKA, R. E. & NAGIB, H. M. 1981 Instabilities in near field of turbulent jets and their dependence on initial conditions and reynolds number. *Tech. Rep.* R-81-2. IIT Fluids & Heat Transfer Report.

ERM, P. L. & JOUBERT, P. N. 1991 Low-Reynolds-number turbulent boundary layers. *J. Fluid Mech.* **230**, 1–44.

FAUCONNIER, D., BOGEY, C. & DICK, E. 2013 On the performance of relaxation filtering for large-eddy simulation. *J. Turbul.* **14** (1), 22–49.

FERNHOLZ, H. H. & FINLEY, P. J. 1996 The incompressible zero-pressure-gradient turbulent boundary layer: an assessment of the data. *Prog. Aerosp. Sci.* **32** (4), 245–311.

FIELDLER, H. E. 1988 Coherent structures in turbulent flows. *Prog. Aerosp. Sci.* **25**, 231–269.

FISHER, M. J., HARPER-BOURNE, M. & GLEGG, S. A. L. 1977 Jet engine noise source location: the polar correlation technique. *J. Sound Vib.* **51** (1), 23–54.

FLEURY, V. 2006 Superdirectivité, bruit d'appariement et autres contributions au bruit de jet subsonique. PhD thesis, Ecole Centrale de Lyon, no. 2006-18.

FLEURY, V., BAILLY, C., JONDEAU, E., MICHARD, M. & JUVÉ, D. 2008 Space–time correlations in two subsonic jets using dual particle image velocimetry measurements. *AIAA J.* **46** (10), 2498–2509.

FONTAINE, R. A., ELLIOTT, G. S., AUSTIN, J. M. & FREUND, J. B. 2015 Very near-nozzle shear-layer turbulence and jet noise. *J. Fluid Mech.* **770**, 27–51.

GLOERFELT, X. & BERLAND, J. 2012 Turbulent boundary layer noise: direct radiation at Mach number 0.5. *J. Fluid Mech.* **723**, 318–351.

GUTMARK, E. & HO, C.-M. 1983 Preferred modes and the spreading rates of jets. *Phys. Fluids* **26** (10), 2932–2938.

HARPER-BOURNE, M. 2010 Jet noise measurements: past and present. *Intl J. Aeroacoust.* **9** (4–5), 559–588.

HILL, W. G., JENKINS, R. C. & GILBERT, B. L. 1976 Effects of the initial boundary-layer state on turbulent jet mixing. *AIAA J.* **14** (11), 1513–1514.

HO, C. & HUERRE, P. 1984 Perturbed free shear layers. *Annu. Rev. Fluid Mech.* **16**, 365–422.

HUSAIN, Z. D. & HUSSAIN, A. K. M. F. 1979 Axisymmetric mixing layer: influence of the initial and boundary conditions. *AIAA J.* **17** (1), 48–55.

HUSSAIN, A. K. M. F. 1986 Coherent structures and turbulence. *J. Fluid Mech.* **173**, 303–356.

HUSSAIN, A. K. M. F. & ZAMAN, K. B. M. Q. 1985 An experimental study of organized motions in the turbulent plane mixing layer. *J. Fluid Mech.* **159**, 85–104.

HUSSAIN, A. K. M. F. & ZEDAN, M. F. 1978*a* Effects of the initial condition on the axisymmetric free shear layer: effects of the initial fluctuation level. *Phys. Fluids* **21** (9), 1475–1481.

HUSSAIN, A. K. M. F. & ZEDAN, M. F. 1978*b* Effects of the initial condition on the axisymmetric free shear layer: Effects of the initial momentum thickness. *Phys. Fluids* **21** (7), 1100–1112.

HUTCHINGS, N. 2012 Caution: tripping hazards. *J. Fluid Mech.* **710**, 1–4.

KARON, A. Z. & AHUJA, K. K. 2013. Effect of nozzle-exit boundary layer on jet noise. *AIAA Paper* 2013-0615.

KIM, J., MOIN, P. & MOSER, R. 1987 Turbulence statistics in fully developed channel flow at low Reynolds number. *J. Fluid Mech.* **177**, 133–166.

KLEBANOFF, P. S. & DIEHL, Z. W. 1952. Some features of artificially thickened fully developed turbulent boundary layers with zero pressure gradient. *NACA Tech. Rep.* 1110.

KREMER, F. & BOGEY, C. 2015 Large-eddy simulation of turbulent channel flow using relaxation filtering: resolution requirement and Reynolds number effects. *Comput. Fluids* **116**, 17–28.

LAU, J. C., MORRIS, P. J. & FISHER, M. J. 1979 Measurements in subsonic and supersonic free jets using a laser velocimeter. *J. Fluid Mech.* **93** (1), 1–27.

LEE, S. S. & BRIDGES, J. 2005. Phased-array measurements of single flow hot jets. *NACA Tech. Rep.* 2005-213826.

LILLEY, G. M. 1994 Jet noise classical theory and experiments. In *Aeroacoustics of Flight Vehicles* (ed. H. H. Hubbard), vol. 1, pp. 211–289. Acoustical Society of America.

LORTEAU, M., CLÉRO, F. & VUILLOT, F. 2015 Analysis of noise radiation mechanisms in hot subsonic jet from a validated large eddy simulation solution. *Phys. Fluids* **27** (7), 075108.

MAESTRELLO, L. & MCDAID, E. 1971 Acoustic characteristics of a high-subsonic jet. *AIAA J.* **9** (6), 1058–1066.

MICHALKE, A. 1984 Survey on jet instability theory. *Prog. Aerosp. Sci.* **21**, 159–199.

MOHSENI, K. & COLONIUS, T. 2000 Numerical treatment of polar coordinate singularities. *J. Comput. Phys.* **157** (2), 787–795.

MOLLO-CHRISTENSEN, E., KOLPIN, M. A. & MARTUCELLI, J. R. 1964 Experiments on jet flows and jet noise far-field spectra and directivity patterns. *J. Fluid Mech.* **18** (2), 285–301.

MONTY, J. P., HUTCHINS, N., NG, H. C. H., MARUSIC, I. & CHONG, M. S. 2009 A comparison of turbulent pipe, channel and boundary layer flows. *J. Fluid Mech.* **632**, 431–442.

MORRIS, P. J. 1976 The spatial viscous instability of axisymmetric jets. *J. Fluid Mech.* **77** (3), 511–529.

MORRIS, P. J. 2010 The instability of high speed jets. *Intl J. Aeroacoust.* **9** (1–2), 1–50.

MORRIS, P. J. & ZAMAN, K. B. M. Q. 2009 Velocity measurements in jets with application to noise source modelling. *J. Sound Vib.* **329** (4), 394–414.

MORRIS, S. C. & FOSS, J. F. 2003 Turbulent boundary layer to single-stream shear layer: the transition region. *J. Fluid Mech.* **494**, 187–221.

NARAYANAN, S., BARBER, T. J. & POLAK, D. R. 2002 High subsonic jet experiments: Turbulence and noise generation studies. *AIAA J.* **40** (3), 430–437.

PANDA, J., SEASHOLTZ, R. G. & ELAM, K. A. 2005 Investigation of noise sources in high-speed jets via correlation measurements. *J. Fluid Mech.* **537**, 349–385.

RAMAN, G., RICE, E. J. & RESHOTKO, E. 1994 Mode spectra of natural disturbances in a circular jet and the effect of acoustic forcing. *Exp. Fluids* **17**, 415–426.

RAMAN, G., ZAMAN, K. B. M. Q. & RICE, E. J. 1989 Initial turbulence effect on jet evolution with and without tonal excitation. *Phys. Fluids* A **1** (7), 1240–1248.

RUSS, S. & STRYKOWSKI, P. J. 1993 Turbulent structure and entrainment in heated jets: the effect of initial conditions. *Phys. Fluids* A **5** (12), 3216–3225.

SABATINI, R. & BAILLY, C. 2015 Numerical algorithm for computing acoustic and vortical spatial instability waves. *AIAA J.* **53** (3), 692–702.

SANDBERG, R. D., SANDHAM, N. D. & SUPONITSKY, V. 2012 DNS of compressible pipe flow exiting into a coflow. *Intl J. Heat Fluid Flow* **35**, 33–44.

SATO, H. 1971 Experimental investigation on the transition of laminar separated layer. *J. Phys. Soc. Japan* **48**, 702–709.

SCHLATTER, P. & ÖRLÜ, R. 2012 Turbulent boundary layers at moderate Reynolds numbers: inflow length and tripping effects. *J. Fluid Mech.* **710**, 5–34.

SCHUBAUER, G. B. & KLEBANOFF, P. S. 1955. Contributions on the mechanics of boundary-layer transition. *NACA Tech. Rep.* 3498.

SPALART, P. R. 1988 Direct simulation of a turbulent boundary layer up to $r_\theta = 1410$. *J. Fluid Mech.* **187**, 61–98.

TAM, C. K. W. 1998 Jet noise: since 1952. *Theor. Comput. Fluid Dyn.* **10** (1-4), 393–405.

TAM, C. K. W. & DONG, Z. 1996 Radiation and outflow boundary conditions for direct computation of acoustic and flow disturbances in a nonuniform mean flow. *J. Comput. Acoust.* **4** (2), 175–201.

TAM, C. K. W., VISWANATHAN, K., AHUJA, K. K. & PANDA, J. 2008 The sources of jet noise: experimental evidence. *J. Fluid Mech.* **615**, 253–292.

TANNA, H. K. 1977 An experimental study of jet noise. Part I: Turbulent mixing noise. *J. Sound Vib.* **50** (3), 405–428.

TOMKINS, C. D. & ADRIAN, R. J. 2005 Energetic spanwise modes in the logarithmic layer of a turbulent boundary layer. *J. Fluid Mech.* **545**, 141–162.

UZUN, A. & HUSSAINI, M. 2007 Investigation of high frequency noise generation in the near-nozzle region of a jet using large eddy simulation. *Theor. Comput. Fluid Dyn.* **21** (4), 291–321.

VISWANATHAN, K. 2004 Aeroacoustics of hot jets. *J. Fluid Mech.* **516**, 39–82.

VISWANATHAN, K. 2006 Distributions of noise sources in heated and cold jets: are they different? *Intl J. Aeroacoust.* **9** (4–5), 589–625.

VISWANATHAN, K. & CLARK, L. T. 2004 Effect of nozzle internal contour on jet aeroacoustics. *Intl J. Aeroacoust.* **3** (2), 103–135.

WYGNANSKI, I., OSTER, D., FIEDLER, H. & DZIOMBA, B. 1979 On the perseverance of a quasi-two-dimensional eddy-structure in a turbulent mixing layer. *J. Fluid Mech.* **93** (2), 325–335.

XU, G. & ANTONIA, R. A. 2002 Effects of different initial conditions on a turbulent free jet. *Exp. Fluids* **33**, 677–683.

YULE, A. J. 1978 Large-scale structure in the mixing layer of a round jet. *J. Fluid Mech.* **89** (3), 413–432.

ZAMAN, K. B. M. Q. 1985*a* Effect of initial condition on subsonic jet noise. *AIAA J.* **23** (9), 1370–1373.

ZAMAN, K. B. M. Q. 1985*b* Far-field noise of a subsonic jet under controlled excitation. *J. Fluid Mech.* **152**, 83–111.

ZAMAN, K. B. M. Q. 1986 Flow field and near and far sound field of a subsonic jet. *J. Sound Vib.* **106** (1), 1–16.

ZAMAN, K. B. M. Q. 2012 Effect of initial boundary-layer state on subsonic jet noise. *AIAA J.* **50** (8), 1784–1795.

ZAMAN, K. B. M. Q. 2017. Increased jet noise due to a 'nominally laminar' state of nozzle exit boundary layer. *NASA Tech. Rep.* 2017-219440.

ZAMAN, K. B. M. Q. & HUSSAIN, A. K. M. F. 1981 Turbulence suppression in free shear flows by controlled excitation. *J. Fluid Mech.* **103**, 133–159.

ZHU, M., PÉREZ ARROYO, C., FOSSO POUANGUÉ, A., SANJOSÉ, M. & MOREAU, S. 2018 Isothermal and heated subsonic jet noise using large eddy simulations on unstructured grids. *Comput. Fluids* **171**, 166–192.